



Contents lists available at ScienceDirect

Remote Sensing of Environment

journal homepage: www.elsevier.com/locate/rse

Modeling the radiation regime of a discontinuous canopy based on the stochastic radiative transport theory: Modification, evaluation and validation

Kai Yan^{a,b,f,*}, Yiman Zhang^{a,*}, Yiyi Tong^b, Yelu Zeng^c, Jiabin Pu^a, Si Gao^a, Linyuan Li^b, Xihan Mu^b, Guangjian Yan^b, Miina Rautiainen^{d,e}, Yuri Knyazikhin^f, Ranga B. Myneni^f

^a School of Land Science and Techniques, China University of Geosciences, Beijing 100083, China

^b State Key Laboratory of Remote Sensing Science, Jointly Sponsored by Chinese Academy of Sciences and Beijing Normal University, Beijing 100101, China

^c Department of Global Ecology, Carnegie Institution for Science, Stanford, CA 94305, USA

^d Department of Built Environment, Aalto University, School of Engineering, P.O. Box 14100, FI-00076 Aalto, Finland

^e Department of Electronics and Nanoengineering, Aalto University, School of Electrical Engineering, P.O. Box 15500, FI-00076 Aalto, Finland

^f Department of Earth and Environment, Boston University, Boston, MA 02215, USA

ARTICLE INFO

Editor: Jing M. Chen

Keywords:

Stochastic radiative transfer (SRT)
Radiation regime
Vegetation canopy
Evaluation and validation
Hotspot effect

ABSTRACT

Canopy radiative transfer (RT) modeling is critical for the quantitative retrieval of vegetation biophysical parameters and has been under intensive research over the decades. RT models of discontinuous canopies, such as three-dimensional (3D) RT models, posed challenges for the early one-dimensional (1D) hypothesis. Although 3D RT models have higher accuracy, theoretically, they suffer from two problems: detailed scene parameters and complex computational steps. To overcome these problems, the stochastic radiative transfer (SRT) theory, which is known to have the accuracy of 3D RT while being as simple as 1D RT, has been adapted from atmospheric research to the study of vegetation canopies. While the SRT model has been adopted into the operational production of vegetation parameters, its accuracy needs further improvement because of the insufficient consideration of hotspot effects. Additionally, the evaluation and validation of SRT process are still preliminary, which hinders its further development and application. To provide the community with missing information and a scientific basis for subsequent model improvement, we modified, evaluated, and validated the SRT model in this study. First, we proposed the new version of SRT model to better achieve the coupling of SRT process and hotspot effect by dividing the previous SRT into four subproblems. Then, we evaluated the performance of the modified SRT by comparing multiple intermediate variables in the SRT process with 3D computer simulations, and analyzed the model sensitivity to key input parameters as well as the spatial distribution and conservation of radiation energy. Our findings reconfirmed that the SRT theory can well describe the radiation regime of discontinuous canopies with balanced efficiency and accuracy. Moreover, the newly proposed coupling scheme of hotspot effect further improves the model performance in the hotspot regions. Finally, the unmanned aerial vehicle (UAV) observations served as a reference to validate the modeled canopy reflectance, which shows a high concordance. These results provide a detailed theoretical basis for applications and further improvements of the SRT model.

1. Introduction

Vegetation canopy structure determines the radiation regime of a plant and its biochemical functions. Therefore, information about canopy structure parameters is essential for evaluating chlorophyll content, net primary productivity, and biodiversity (Chen et al., 2003; Jiao et al.,

2016; Lee et al., 2017; Y. Xiao et al., 2014). The past decades have witnessed the rapid development of remote sensing instruments and technologies (Comerón et al., 2017; Diner et al., 2013; Jawak and Luis, 2013; Lechner et al., 2020; Peral et al., 2018). Traditional optical satellite-borne sensors such as moderate resolution imaging spectroradiometer (MODIS) and advanced very high resolution radiometer

* Corresponding authors at: School of Land Science and Techniques, China University of Geosciences, Beijing 100083, China.

E-mail addresses: kaiyan@cugb.edu.cn (K. Yan), yiman@cugb.edu.cn (Y. Zhang).

<https://doi.org/10.1016/j.rse.2021.112728>

Received 15 April 2021; Received in revised form 14 August 2021; Accepted 28 September 2021

0034-4257/© 2021 Elsevier Inc. All rights reserved.

(AVHRR), have been continuously monitoring the Earth's surface vegetation for over decades due to their high revisit frequency and wide coverage. However, these sensors measure only the mean reflectances of heterogeneous canopy limited by the finite pixel sizes rather than the vegetation structure parameters (Huang et al., 2018; Kern et al., 2020; Venturini et al., 2004). Therefore, remote sensing signals need to be linked with vegetation parameters through a retrieval process that involves either empirical-statistical models, semi-empirical models or physical models (Houborg et al., 2007; Rasmus et al., 2015; Vuolo et al., 2013).

Empirical-statistical models, such as the Shibayama model (Shibayama and Wiegand, 1985) and the Walthall model (Walthall et al., 1985), semi-empirical models, such as CLAIR model (Clevers, 1989), usually have a simple form that do not need to physically explain the relationship between the statistical characteristics of radiation field and the corresponding canopy structure. In particular, machine learning regression algorithms have been applied to improve the retrieval accuracy of traditional empirical/semi-empirical models in recent years (Baret et al., 2013; Verrelst et al., 2012; Z. Xiao et al., 2014). However, the empirical coefficients in these models' expression vary with crown types, background and other factors, and the physical processes they involved are not always known, which hinders the better application of these models in regional and global remote sensing (Colombo et al., 2003; Goel, 1988). In contrast to the empirical models, physical models are based on clear physical meanings, providing a physical description for the process of the interaction between incident radiation streaming and the canopy (Houborg et al., 2007).

The most direct way to describe the interactions between incident radiation and the canopy is computer simulation based on the three-dimensional (3D) radiative transfer (RT) theory, such as discrete anisotropic radiative transfer (DART) (Gastellu-Etchegorry et al., 2015) and large scale remote sensing data and image simulation framework (LESS) (Qi et al., 2019). Since computer simulation models describe clear physical process and have high accuracy, they are always used as a reference to validate other models (Pu et al., 2020; G. Yan et al., 2021; K. Yan et al., 2021a). However, 3D simulations involve a large number of computational steps and detailed information about scene structure (Jacquemoud et al., 1997), thus computer simulation models are not convenient for parameter retrieval. To reduce the computational cost, the RT problem has been solved using the average characteristics obtained by averaging over the 3D canopy structure. This technique led to a family of one-dimensional (1D) models obtained using various averaging procedures (Suits, 1971; Verheof, 1984; Yin et al., 2017). This simplification however makes such models insensitive to 3D effects of canopy structure.

To develop RT models that are sensitive to 3D canopy structure and computationally efficient, a stochastic approach originally developed in cloud physics (Georgi, 1990; Vainikko, 1973a, 1973b) was adapted (Huang et al., 2008; Shabanov et al., 2000; K. Yan et al., 2021c; Yin et al., 2015). The stochastic radiative transfer equation (SRTE) in vegetation studies aims to derive a close system of simple equations that contain the ensemble-average radiance and its unknowable moments. Unlike the 1D approach, the stochastic approach estimates the 3D radiative field in the vegetation canopy first and then averages it to obtain the ensemble average radiance and higher statistical moments. This imparts sensitivity of the stochastic radiative transfer (SRT) model to 3D structure effects, and the computational cost is comparable to the conventional 1D radiative transfer equation (RTE).

Due to the nice balance of efficiency and accuracy, the SRT model has been used to account for a mixture of multiple vegetation species with different structural parameters and optical properties (Shabanov et al., 2007) and to study the mixture scenes of multiple continuous or discontinuous vegetation cover types (Zeng et al., 2020b), providing a new analytical way for heterogeneous landscapes to retrieve the biophysical parameters. The analytical fluorescence RT model was proposed based on the outputs of the SRT model to investigate the effects of

canopy structure and observation geometry on solar-induced chlorophyll fluorescence (SIF) (Zeng et al., 2020a), and it has been extended to study the heterogeneous distribution of damaged leaves, leading the way to potential future quantitative retrievals of damaged vegetation (Li et al., 2020). Moreover, the SRT model has also been applied into the operational retrieval of the leaf area index (LAI) and fraction of absorbed photosynthetically active radiation (FPAR) for savannas (biome type 4 in the product) in MODIS series of vegetation products (Kotchenova et al., 2003; Pu et al., 2020; Shabanov et al., 2003, 2005, 2007; Yan et al., 2018). Previous studies found that the LAI/FPAR accuracy and stability of SRT-based biome type are comparable to that of the 3D RT-based biome types (K. Yan et al., 2021b; Yan et al., 2016a, 2016b).

Contrary to the RT model assumption that the canopy elements are turbid medium, the plant leaves have a finite size in nature. Thus the RT model cannot characterize the hotspot effects (i.e., the reflectance reaches a maximum when the view direction coincides with the illumination direction) (Qin and Xiang, 1994; Suits, 1971). As an RT model with a special form, the original version of the SRT model (hereafter referred to as the SRT_HSO) does not consider the hotspot effects, resulting in an obvious bias of canopy bidirectional reflectance factors (BRFs) within a certain range in the hotspot direction. To solve this, Kuusk (1985) approach was adopted to consider the hotspot effect by multiplying the extinction coefficient with a semi-empirical parameter (hereafter referred to as the SRT_HS1). However, the SRT_HS1 model has two theoretical defects in the hotspot modeling: 1) the hotspot correction was applied on extinction coefficients for both single and multiple scatterings, and ignored the fact that multiple scattered photons do not cause the hotspot effects. 2) The hotspot effect caused by directly illuminated soil was not considered. Thus, there is a significant need to make up these defects by modifying the SRT_HS1 model to better capture the hotspot effects. This is the first objective of this article.

Moreover, Shabanov et al. (2000, 2007) have analyzed the BRFs in different LAI canopy landscapes and the radiative flux in different species using the SRT model. Followed them, Huang et al. (2008) have evaluated the conditional pair correlation function (PCF) for cylindrical and conical canopies. Although few researches on SRT model have been conducted, we should realize that the evaluation and validation of this model are still preliminary (e.g., the sensitivity analysis to input parameters is lacking, the intermediate variables in the SRT process have not been verified, and the ground validation is limited), which limits further developments and applications of this model. Thus, the second objective of this article is to provide a comprehensive evaluation and detailed validation of the SRT model, which was achieved through computer simulations and an unmanned aerial vehicle (UAV) field campaign.

The following Section 2 and Appendix introduce the SRT basic theory and the hotspot modification efforts. In Section 3, we checked the performance of the new proposed SRT-Hotspot coupling scheme and detailedly evaluated the SRT model through comprehensive comparisons with computer simulations in terms of canopy reflectance, conditional pair-correlation functions (PCF) and recollision probability. Meanwhile, we analyzed the model sensitivity to input parameters, and the energy distribution and conservation in the radiation field. In Section 4, the model validation was conducted through a multi-angular UAV experiment. Conclusion are given in Section 5.

2. Stochastic modeling of the canopy radiation regime

2.1. Basic theory of stochastic radiative transfer

We consider a typical 3D discontinuous vegetation canopy consisting of identical trees for RT calculation and residing in the layer $0 < Z < H$ in the coordinate system (Fig. 1). From a stochastic view, 3D canopy structure is treated as a stochastic process of space and can be described with the indicator function $\chi(x, y, z)$ whose value is 1 if the point (x, y, z) is covered by vegetation and 0 otherwise. The SRTE is derived by

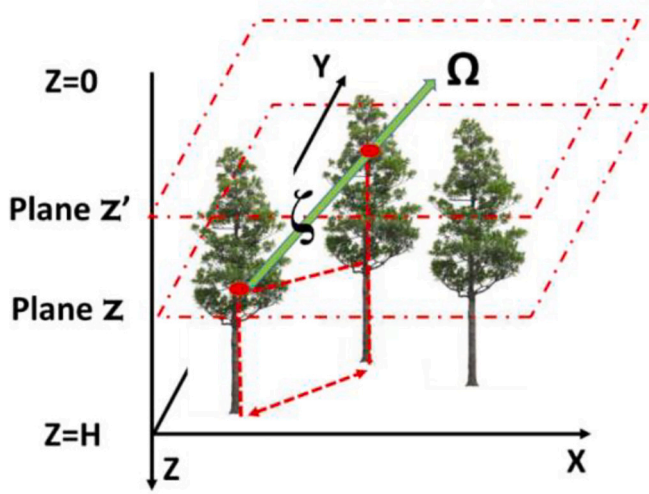


Fig. 1. Illustration of a typical discontinuous vegetation canopy and the coordinate system for stochastic radiative transfer equation (SRTE). The plane $Z = 0$ and $Z = H$ denote the upper and lower boundary of vegetation canopy, respectively. There is a vegetated point at plane Z , which travels in the upward direction Ω (unit vector) for a distance ζ to arrive at plane Z' .

averaging the 3D RT process over the horizontal plane, while it still preserves the impact of a canopy structure on the radiation regime. The SRTE requires to calculate two kinds of mean intensities, one over the whole scene $\bar{I}(z, \Omega)$ and the other over the vegetation occupied area $U(z, \Omega)$. The formulas for the mean intensities $\bar{I}(z, \Omega)$ and $U(z, \Omega)$ at depth z along Ω direction are shown in Eqs. (A1) and (A3). The details about the derivation can be seen in Shabanov et al. (2000). Given the statistical characteristics of a canopy structure, the mean intensities emanating from a radiation field can be measured by the Satellite-borne sensors (Huang et al., 2008).

Generally, the canopy is illuminated by a direct solar beam and diffuse radiation scattered by the atmosphere. Therefore, the horizontal average intensity over the vegetation occupied area $U(z, \Omega)$ or the entire horizontal plane $\bar{I}(z, \Omega)$ can be decomposed into the direct component and the diffuse component of the incoming solar radiation as (Shabanov et al., 2000):

$$U(z, \Omega) = i_0 U_{\text{dir}}(z) \delta(\Omega - \Omega_0) + U_{\text{dif}}(z, \Omega) \quad (1)$$

$$\bar{I}(z, \Omega) = i_0 \bar{I}_{\text{dir}}(z) \delta(\Omega - \Omega_0) + \bar{I}_{\text{dif}}(z, \Omega) \quad (2)$$

where i_0 is the ratio of direct radiation incident on the upper boundary; Ω_0 is the incident direction of direct light and Ω is the view direction; $\delta(\Omega - \Omega_0)$ is Dirac's delta function; $U_{\text{dir}}(z)$ ($\bar{I}_{\text{dir}}(z)$) and $U_{\text{dif}}(z, \Omega)$ ($\bar{I}_{\text{dif}}(z, \Omega)$) are the direct component and diffuse component over the vegetation-occupied area (over the whole scene area), respectively. Further information on the derivation of each part is available in Eqs. (A6)-(A11).

To trace the energy input and output of the system over the vegetation canopy space and in all directions, the mean intensity integral equation is a standard procedure (Eqs. (A1) and (A3)) (Huang et al., 2008). Thus, the energy conservation law can be expressed as a relationship between reflectance, transmittance, and absorbance:

$$R(\lambda) + A(\lambda) + (1 - \rho_{\text{soil}}) * T(\lambda) = 1 \quad (3)$$

where $R(\lambda)$ is the reflectance, $T(\lambda)$ is the transmittance, and $A(\lambda)$ is the absorbance of the whole canopy-soil system (Shabanov et al., 2000, 2007).

2.2. Coupling the SRT and hotspot modeling

In previous research, to save computational effort and to couple the vegetation and soil layers, the whole SRT process was split into two subproblems for analysis: black soil (BS, Figs. 2a-b) and soil (S, Figs. 2c-d) problems. In the BS subproblem, the energy is incident from the canopy top ($Z = 0$), and the soil reflectance (ρ_{soil}) is set to 0. In the S subproblem, there is no illumination at the canopy top, while there is an isotropic source of illumination uniformly distributed at the canopy bottom ($Z = H$). Combining these two problems, the radiation of the whole canopy-soil system is shown in Eqs. (A12)–(A14) (Knyazikhin et al., 1998; Shabanov et al., 2000).

Depending on the incident energy forms, here, we further divided the BS subproblem into two parts: (1) direct incident radiation (BS_Dir) and (2) diffused incident radiation (BS_Diff). Meanwhile, the S subproblem was split into: (3) without photon-vegetation collision (S_NoCollision) and (4) with photon-vegetation collision (S_Collision) according to the energy source of S problem with or without vegetation collision. In summary, this study divided the whole SRT process into four parts, as shown in Fig. 2, specifically:

- (1) Fig. 2a shows that the incident light source is direct light in the BS subproblem (BS_Dir). The light that reaches the soil can be divided into two forms: ① the light will not interact with vegetation and reaches the soil directly; ② the light will be scattered at least one time before reaching the soil. In the process of photon-vegetation interaction, the photons are scattered when they collided with vegetation one (②-1) or more (②-2) times.
- (2) Subproblem BS_Diff indicates the radiation regime when the incident light is diffused light (Fig. 2b). Like the BS_Dir subproblem, the diffused light reaches the soil also have two forms (③ and ④).
- (3) Fig. 2c is an illustration that soil reflects the radiation which has not been scattered by leaves (S_NoCollision). That is to say the energy ① and ④ will be reflected by the soil and become to ⑤.
- (4) S_Collision represents that soil reflects the radiation which has been scattered multiple times (Fig. 2d). In other words, the energy ②, ③ and ⑥ (caused by multiple reflectance between soil and canopy bottom) will be reflected by soil and become to ⑦.

Due to the directionality of energy in the four subproblems and the finite dimension of plant leaves, the so-called hotspot effect occurs when the view direction coincides with the illumination direction (Suits, 1971). In the hotspot direction, photons will escape from the canopy without the extinction effect of the leaves. The standard approach for quantifying the hotspot effect is by modifying the extinction coefficient $\sigma(\Omega)$ as follows (Kuusk, 1985; Ross and Marshak, 1989):

$$\sigma(\Omega, \Omega_0) = \begin{cases} \sigma(\Omega) \left(1 - \sqrt{\frac{G(\Omega_0)|\mu(\Omega)|}{G(\Omega)|\mu(\Omega_0)|}} \exp\left(-\Delta(\Omega, \Omega_0) \frac{H}{S_L}\right) \right), & \text{if } (\Omega, \Omega_0) \leq 0 \\ \sigma(\Omega), & \text{if } (\Omega, \Omega_0) > 0 \end{cases} \quad (4)$$

$$\Delta(\Omega, \Omega_0) = \sqrt{\frac{1}{|\mu^2(\Omega_0)|} + \frac{1}{|\mu^2(\Omega)|} + \frac{2(\Omega_0, \Omega)}{|\mu(\Omega_0)\mu(\Omega)|}} \quad (5)$$

where $G(\Omega_0)$ and $G(\Omega)$ are the mean projections of the leaf normal in the directions Ω_0 and Ω . S_L and H are the leaf linear characteristic dimension and canopy height, and $\Delta(\Omega, \Omega_0)$ is defined by Eq. (5). Therefore, Kuusk approach was adopted to describe the hotspot effects by coupling with the original SRT model (SRT_HS0), that is SRT_HS1 model. In SRT_HS1, the extinction coefficient $\sigma(\Omega)$ was modified as shown in Eq. (4) for the energy ①, ②-1, ②-2 (Fig. 2a), ③-1, ③-2 (Fig. 2b), ⑤ (Fig. 2c) and ⑦ (Fig. 2d). However, we noted that parts ②-2, ③-2 and ⑦ counting for

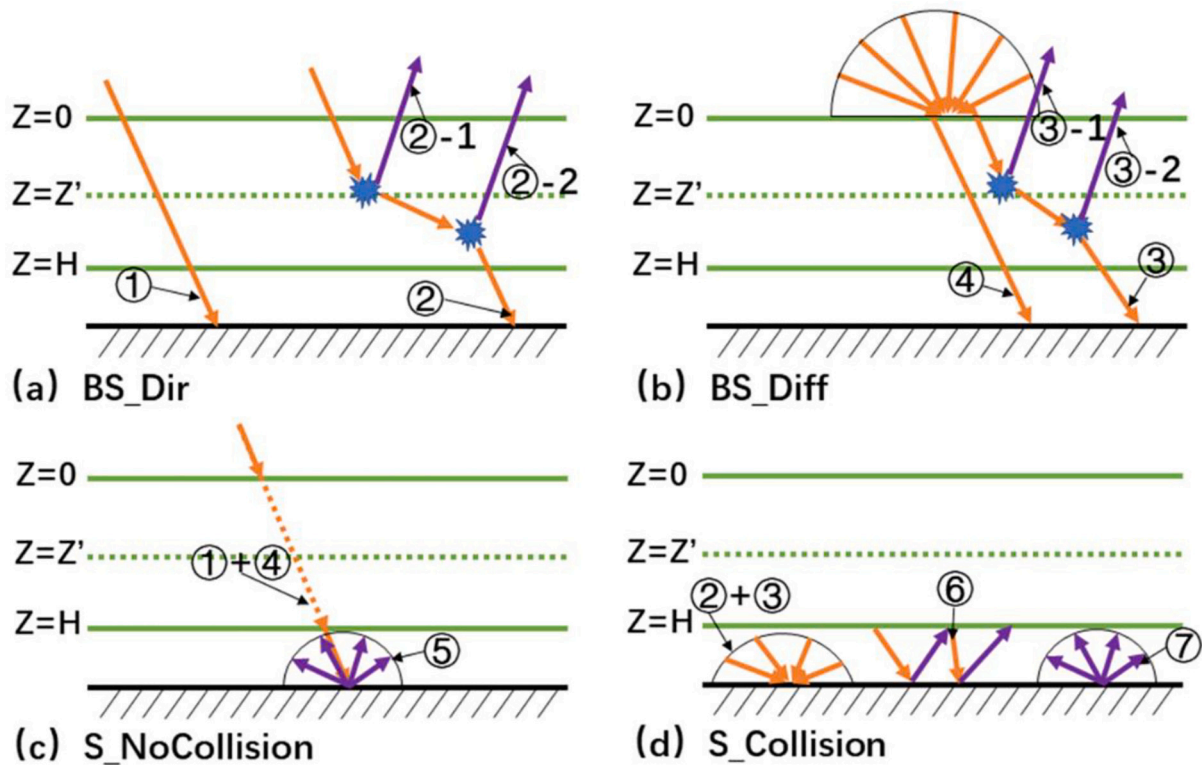


Fig. 2. Illustrations of the four subproblems for the stochastic radiative transfer (SRT) process. Panels a and b show the distribution of incident direct light and diffused light interacting with leaves in the canopy, respectively (black soil problem). Panels c and d show the source and distribution of energy reflected from the soil (soil problem). The symbols ①-⑦ indicate the energy that reaches the soil or is reflected by the soil. The symbols ②-1, ②-2, ③-1 and ③-2 indicate the energy that is reflected by the vegetation. The orange and purple colors represent the incident and reflected energy, respectively. (For interpretation of the references to colour in this figure legend, the reader is referred to the web version of this article.)

the multiple scattering do not contribute to the hotspot effects and were incorrectly modified in SRT-HS1. Moreover, the hotspot contribution from the soil was failed to be considered in SRT-HS1.

Here we tried to make up the above two defects and propose the SRT_HS2 version, where the extinction coefficient $\sigma(\Omega)$ will be modified when the energy is the ①, ②-1 (Fig. 2a), ③-1, ④ (Fig. 2b) and ⑤ (Fig. 2c) parts. Parts ②-1 and ③-1 contribute to vegetation hotspot effect, while parts ①, ④ and ⑤ contribute to soil hotspot effect. Thus, the solution of the whole SRT process is a combination of the solutions of four subproblems: (1) BS_Dir, (2) BS_Diff, (3) S_NoCollision and (4) S_Collision. Finally, the whole scene hemispherical-directional reflectance factors (HDRF) can be expressed as:

$$\begin{aligned}
 HDRF(\Omega_0, \Omega) = & R_{BS_Dir}(\Omega_0, \Omega) + R_{BS_Diff}(\Omega) + \rho_{soil} \cdot \left(T_{BS_Dir}^0(\Omega_0) \right. \\
 & + T_{BS_Diff}^0(\Omega_0) \cdot R_{S_hs}(\Omega_0, \Omega) + \rho_{soil} \left(T_{BS_Dir}^m(\Omega_0) \right. \\
 & + T_{BS_Diff}^m(\Omega_0) \cdot R_S(\Omega) \\
 & + \frac{\rho_{soil}}{1 - \rho_{soil} \cdot R_{V_s}(\lambda)} \cdot \rho_{soil} \cdot R_{V_s}(\lambda) \cdot T_{BS}(\Omega_0) \cdot R_S(\Omega) \quad (6)
 \end{aligned}$$

where $R_{BS_Dir}(\Omega_0, \Omega)$ (②-1 and ②-2) and $R_{BS_Diff}(\Omega)$ (③-1 and ③-2) are the reflectance in the subproblems BS_Dir (Fig. 2a) and BS_Diff (Fig. 2b), respectively. $T_{BS_Dir}^0(\Omega_0)$ and $T_{BS_Diff}^0(\Omega_0)$ denote the canopy transmittance of direct radiation (①) and diffuse radiation (④) with no photon-vegetation collision in the BS subproblem; $T_{BS_Dir}^m(\Omega_0)$ and $T_{BS_Diff}^m(\Omega_0)$ are the canopy transmittance for direct radiation (②) and diffuse radiation (③) with one or multiple times photon-vegetation collision in the BS subproblem, respectively. $R_S(\Omega)$ is the hemispherical-directional reflectance in the S subproblem (⑤ + ⑦ in Fig. 2). $R_{S_hs}(\Omega_0, \Omega)$ is the reflectance in the S_NoCollision subproblem

accounting for the hotspot effect; $R_{V_s}(\lambda)$ is the canopy albedo for the S subproblem. On the right of Eq. (6), the third and fourth terms are the HDRF increment of no collision (⑤) and collision (⑦) portions in the S problem, respectively. The fifth term represents the HDRF increment after multiple reflectance between the soil and the canopy bottom (⑥). Based on the above derivation, the energy conservation law should be checked on each subproblem and total problem as:

$$R_k(\lambda) + A_k(\lambda) + T_k(\lambda) = F_k \quad (7)$$

where k represents four subproblems (BS_Dir, BS_Diff, S_NoCollision and S_Collision) and the total problem. F_k represents incident radiation.

The energy conservation law is a feature of the classical RTE without hotspot modification. However, when the extinction coefficient in the RTE is modified by multiplying a semi-empirical parameter artificially to include the hotspot (Kuusk, 1985), it will result in a disruption of the energy balance, which violates the energy conservation law.

3. Model evaluation

3.1. Comparison of different SRT-hotspot coupling schemes

In Fig. 3, we compared the simulated reflectance in the principal plane from three versions of SRT model. The upper boundary conditions (i.e., direct sunlight ration) changed from 0 (all diffused skylight) to 1 (all direct sunlight). It can be seen that the three versions of SRT model show very good consistency with changing view zenith angle except near the hotspot region. We noted that the original SRT model (SRT-HS0) cannot capture any hotspot phenomenon at any upper boundary condition. In particular, when there is no directional incident sunlight (Fig. 3a), there should be no hotspot phenomenon, while the previous

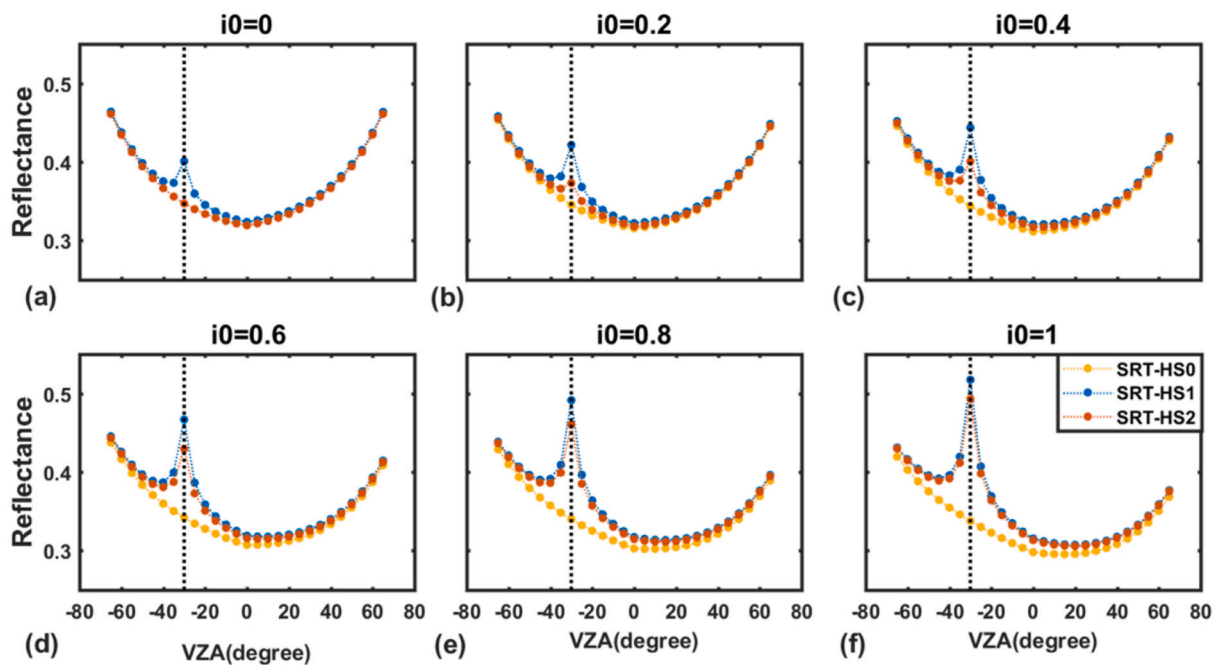


Fig. 3. Comparison of the reflectance from three SRT-Hotspot coupling schemes in different upper boundary conditions. The “SRT_HS0” denotes the original SRT model without the hotspot modification. The “SRT_HS1” denotes previous hotspot modification on both single and multiple scatterings. The “SRT_HS2” denotes our newly proposed SRT-Hotspot coupling scheme. “ i_0 ” is the direct sunlight ratio. The scene consists of identical cylindrical canopies. The tree diameter, height and leaf angle distribution (LAD) are 3 m, 2 m and spherical, respectively. The fractional vegetation cover (FVC) and foliage area volume density (FAVD) are 0.6 and $2m^2/m^3$. The optical parameters of the vegetation and soil can see in Table 1. The solar zenith angle (SZA) and solar azimuth angle are 30° and 0° , respectively.

SRT_HS1 wrongly produced an artificial peak overestimating the reflectance by up to 16% compared with SRT_HS2. As derived in Section 2.2, the energy \odot -2 (Fig. 2a), \odot -2 (Fig. 2b) and \odot are diffused portions without directivity, thus do not lead to hotspot effects. It can be easy to

infer that the differences in hotspot region between SRT_SH1 and SRT_SH2 should gradually decrease as the direct sunlight increases, which is consistent with that shown in Fig. 3. We also noted that when no diffused incident skylight is available (Fig. 3f), there are still some

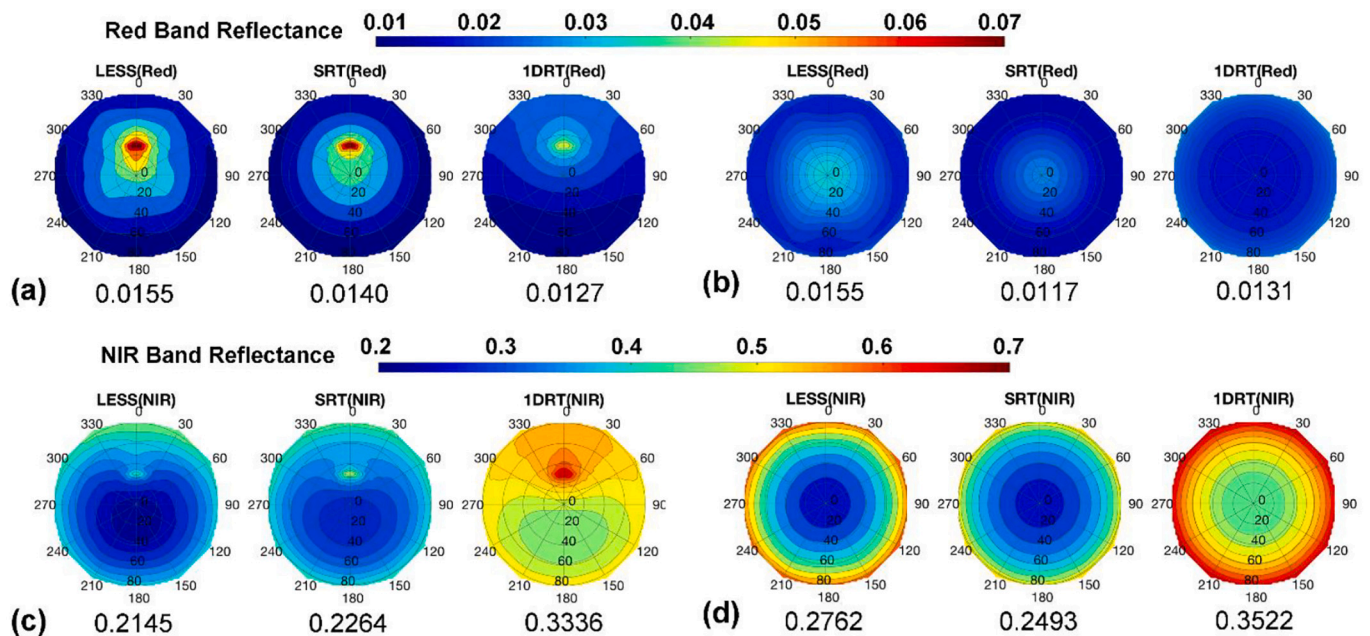


Fig. 4. Comparison of the reflectance from the LESS, 1D RT, and SRT models in the red (top panels) and NIR bands (bottom panels). The input parameters of these models are fractional vegetation cover (FVC: 0.4017), foliage area volume density (FAVD: $3m^2/m^3$), tree height (5 m), leaf angle distribution (LAD: spherical) and crown type (cylinder). In panels a and c, the direct sunlight ratio is 1, whereas in panels b and d, the direct sunlight ratio is 0. The radius of each polar coordinate represents the view zenith angle (VZA), and the azimuth represents the view azimuth angles (VAA). The numbers below each plot represents the mean reflectance in all directions. The optical parameters for this simulation are as in Table 1. (For interpretation of the references to colour in this figure legend, the reader is referred to the web version of this article.)

visible differences between SRT-HS1 and SRT-HS2, which is due to the fact that the extinction coefficient of multiple scattering in SRT-HS1 is wrongly modified and the SRT-HS1 does not consider the hotspot effect caused by soil.

3.2. Variable comparison with computer simulations

3.2.1. BRF comparison with 1D and 3D RT models

The SRT model combines the advantages of the 1D RT and 3D RT models. Thus, the SRT model accuracy should be higher than 1D RT model for discontinuous canopy. Here, we compared the reflectance from 1D RT, SRT, and 3D RT models. In this test, the 1D RT is a special case of SRT when fractional vegetation cover (FVC) is set to 1. The used 3D RT model is the LESS model, which is a newly proposed but well validated model based on photon tracing method.

Fig. 4 shows the polar coordinate plots comparing BRFs generated by the LESS, SRT, and 1D RT models in red and near infrared (NIR) bands with different upper boundary conditions. The scene with FVC and FAVD of 0.4017 and $3 \text{ m}^2/\text{m}^3$, respectively, is consisted of the same cylinder crowns (with spherical leaf angle distribution) that obey a Poisson distribution. The woody elements are not considered in the simulation. The optical properties of leaf and soil are shown in Table 1. It can be observed that the hotspot effects are more obvious in NIR band than in red band. In addition, it is clear that, compared with LESS and SRT, the 1D RT overestimates canopy reflectance in NIR band. This is mainly because that in NIR band, the radiation energy is dominated by multiple scattering among leaves and between canopy and soil, and the 1D RT assumes that the vegetation canopy is horizontally homogeneous without large gaps among crowns.

Moreover, we used the coefficient of determination (R^2) and the root mean square error (RMSE) of LESS vs. 1D RT and LESS vs. SRT as the uncertainty metrics for evaluating the 1D RT and SRT models accuracy. Fig. 5 shows the comparative statistical results of three models with changing direct sunlight ratio and FVC. The RMSE of SRT vs. LESS is less than 0.001 for red band and less than 0.03 for NIR band. However, the RMSE of 1D RT vs. LESS is much larger in both red and NIR bands. In addition, the R^2 of SRT vs. LESS are larger than 0.8 in both bands, and it indicates that the consistency of SRT vs. LESS is better than 1D RT vs. LESS.

3.2.2. Conditional pair-correlation function

The conditional pair-correlation function (PCF) $K(z, z', \Omega)$, an important parameter in SRT model, provides a quantitative description of the canopy structure, which is a probability from a given vegetation point at depth $Z = Z' + \Delta Z$ to find vegetation at depth Z' along a given upward view direction Ω based on a stochastic geometry theory. Here Δz is a vertical distance between two leaf elements in the vegetation canopy. The conditional PCF can be represented as $K(z, z', \Omega) = q(z, z', \Omega)/p(z)$. $q(z, z', \Omega)$, pair-correlation function (PCF), is the probability of simultaneously finding vegetation at canopy depth Z and Z' , and $p(z)$ is the FVC at canopy depth Z (Eq. (A2)). To evaluate the ability of the conditional PCFs on the description of the canopy structure, we compared the conditional PCFs with Monte Carlo (MC) simulation. Fig. 6 shows examples of $K(z, z', \Omega)$ generated by the SRTE and MC simulation, for different crown shapes (Cylindrical, Conical, Ellipsoidal, and Spherical). MC simulation (Disney et al., 2000) needs to generate a random number n (tree numbers) within a fixed scene, and n should obey Poisson distribution $P(n) = (\bar{n})^n \exp(-\bar{n})/n!$ and the locations of n

Table 1
Optical properties of leaf and soil.

Parameters	NIR band	Red band
Leaf reflectance	0.4957	0.0546
Leaf transmittance	0.4409	0.0149
Soil reflectance	0.1590	0.1270

trees obey uniform spatial distribution. Then given the parameters Z , Z' and Ω , one calculates a non-zero value of $\chi(x, y, z)\chi(x', y', z')$ for each realization of the scene. The ensemble-average values of these realizations are assigned to PCF. $p(z)$ is the number of random numbers per unit area at depth Z . According to Eq. (A5), the conditional PCF $K(z, z', \Omega)$ can be analytically calculated and details about the process of modeling the conditional PCF by the MC method can be found in Huang et al. (2008).

The $K(z, z', \Omega)$ calculated by a formula is generally close to the one generated via MC for a vertical solid crown of identical shape in a landscape (this landscape consisted of identical trees resided in the layer 0-H (Fig. 1)). However, the small discrepancy can be identified in Fig. 6, which is attributed to the different simulation principles of MC approach (based on the Poisson distribution) and formulas calculation (based on the stochastic geometry principles). We also found that different crown shapes can lead to different conditional PCFs. Moreover, several other important features were significant. The first feature is the value of the horizontal distance λ when the $K(z, z', \Omega)$ reaches its minimum, which is related to the crown diameter Db at the depth Z (Huang et al., 2008). There is a special value of $K(z, z', \Omega)$, which reaches its minimum ($K(z, z', \Omega) = 0.3$) when the horizontal distance λ of the radiation traversing a cylindrical crown is equal to the diameter Db of the crown ($\lambda/Db = 1$). That is because the Db of the cylindrical crown does not change with the crown height. As the horizontal distance increases, the value of $K(z, z', \Omega)$ changes from a minimum value to a constant value, which is the FVC (Huang et al., 2008). Another feature is that the values $K(z, z', \Omega)$ for the ellipsoidal and spherical crown tend to zero. This is because the Db of an ellipsoidal or spherical crown shows a tendency of increasing first and then decreasing with increasing canopy depth; when Db tends to zero at the canopy depth Z' , $q(z, z', \Omega)$ tends to zero according to Eq. (A4), and $K(z, z', \Omega)$ tends to zero according to Eq. (A5).

3.2.3. Recollision probability

Photon recollision probability is defined as the probability that photons will interact with vegetation within the canopy again, rather than escape from the canopy after photons have interacted with the canopy elements once (Smolander and Stenberg, 2005). The recollision probability can be considered as a function of scattering order N (Lewis and Disney, 2007; Möttus, 2007; Yang et al., 2017). This function is defined as the following:

$$N \sim 1/(1 - p\omega) \quad (8)$$

where ω is the leaf scattering albedo and p is a recollision probability at the saturation (i.e., when scattering order is infinity).

Based on the relationship between the recollision probability and the canopy structural parameters, Tian et al. (2003) developed algorithms for retrieving LAI and FPAR in remote sensing applications. Moreover, the recollision probability is equal to the maximum eigenvalue of the RTE (Knyazikhin et al., 2011). Therefore, exploring the relationship between canopy structural parameters and recollision probability will help achieve better understanding of RTE. In SRT, the recollision probability can be expressed as $p = F_N/\omega F_{N-1}$, and F_N is the scattered order N average irradiance on leaf sides. F_N is a variable related to the SRT model input parameters (including crown shape, crown height, FAVD, leaf angle distribution (LAD), and FVC etc.). More detailed principles for the estimation of p at different scattering orders N by the SRTE model can be found in Yang et al. (2017). The recollision probability changes with the scattered orders N for the different canopy structure parameters are shown in Fig. 7 caption.

Our findings suggest that FVC (Fig. 7b) and FAVD (Fig. 7c) have a great effect on the recollision probability. As the FVC and FAVD increase, the recollision probability gradually increases, which is attributed to more interaction between the radiation and vegetation in the canopy. Furthermore, the crown types also have a great effect on the recollision probability, especially the conical crowns (Fig. 7d).

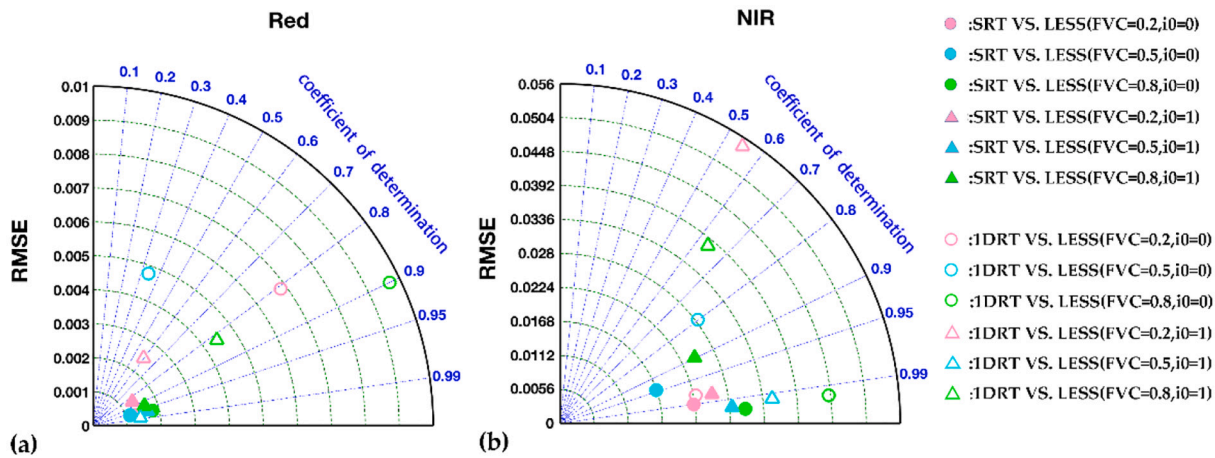


Fig. 5. Performance comparison between SRT and 1D RT using LESS simulation as reference. Panel a is for the red band and panel b is for the NIR band. Three levels of fractional vegetation cover (FVC) and two kinds of incident light were studied. Pink, blue, and green represent the FVC 0.2, 0.5 and 0.8, respectively. The circle and triangle symbols represent the direct light ratio of 0 and 1, respectively. The hollow symbols represent the root mean square error (RMSE) and coefficient of determination (R^2) of 1D RT vs. LESS, and the solid symbols represent the RMSE and R^2 of SRT vs. LESS. (For interpretation of the references to colour in this figure legend, the reader is referred to the web version of this article.)

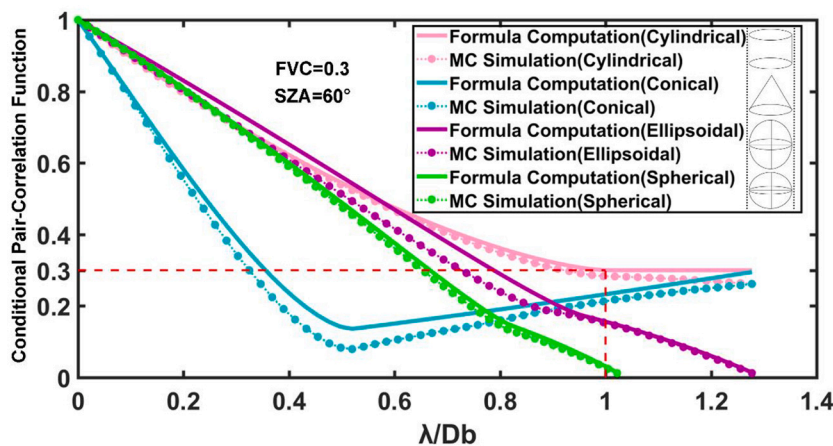


Fig. 6. Comparison of the conditional pair-correlation functions (PCFs) $K(z, z', \Omega)$ (Eq. (A5)) from formula computation (solid lines) and Monte Carlo (MC) simulation (dotted lines). The fractional vegetation cover (FVC), solar azimuth angle (SAA) and solar zenith angle (SZA) are 0.3, 90° and 60° , respectively. The horizontal axis shows values of λ/Db (Db is the maximal diameter of the crown and $\lambda = |z - z'| * \tan(SZA)$ is the horizontal distance between two leaf elements in the canopy (the horizontal projection of $\zeta = |z - z'| / \cos(SZA)$ in Fig. 1)). Here plane Z' is $Z - \Delta z$ and Δz is vertical distance between two leaf elements in the canopy. Pink, blue, purple, and green indicate different crown shapes (Cylindrical, Conical, Ellipsoidal, and Spherical, respectively). The Db of each type crown is 16 m, and the crown height of cylindrical, conical, and ellipsoidal are 20 m ($Z = 20m$) while spherical is 16 m ($Z = 16m$). (For interpretation of the references to colour in this figure legend, the reader is referred to the web version of this article.)

Consistent with the finding of Smolander and Stenberg (2005), the SZA and LAD have minimal effects on the recollision probability (Fig. 7a and e).

The LESS model is a novel 3D RT model based on the ray-tracing theory. The specific simulation steps are as follows: First, a scene was constructed using the identical cylinder crown. Then, some basic parameters were inputted including sun-sensor geometry, illumination conditions, and optical properties of leaf and soil parameters (optical parameters see in Table 1, other parameters see Fig. 7 caption). Since the number of photons can be counted during the propagation throughout the scene, the recollision probability can be expressed as $p = M' / \omega M$, where M and M' are the number of photons before and after the propagation process (Qi et al., 2019). The simulation result reveals that recollision probability changes with the number of iterations from the LESS and SRT model (Fig. 7f). When the iteration number is small, the recollision probability of LESS is lower than SRT. This is because the SRT model averages the value of multiple realizations, while the LESS model uses a random value that represents one realization based on a fixed real scene. As the number of iterations increases, the simulations of the SRT model tend to be consistent with those of the LESS model. Moreover, we found that the SRT results are slightly higher than the LESS simulation when FVC is 0.4. As the FVC increases, the SRT results are slightly lower than the LESS simulation. The most likely reason is that SRT model

considers the mean intensities of an assumed 3D solid crown. We also found, when the FVC increases, the recollision probability increases with the LESS and SRT models for a fixed iteration. This is because the radiation interacts more with vegetation as the FVC increases. This result is consistent with Fig. 7b.

3.3. Sensitivity to key input parameters

To further analyze the sensitivity of the SRT model, we designed a set of single factor experiments aimed to explore the relationship between retrieval uncertainty and model input parameters (i.e., illumination conditions, FAVD, FVC, LAD, crown types, and leaf and soil optical properties). The SZA was fixed at 30° and the SAA was fixed at 0° for all scenes in the sensitivity experiments. For each set of experiments, the parameters are shown in Fig. 8 caption. When the incident diffused light ratio is 0, there is a strong hotspot effect. With the increase of the incident diffused light, the hotspot effect decreases. When the ratio of incident diffused light is 1, the hotspot effect can be neglected in vegetation, as demonstrated by Fig. 2, Fig. 4 and Fig. 8a. This indicates that the changes of sunlight have a great effect on vegetation reflectance. When the observed area expands from the hotspot direction, the reflectance shows a tendency of decreasing firstly then increasing. As the FVC or FAVD increases, the whole scene reflectance gradually increases

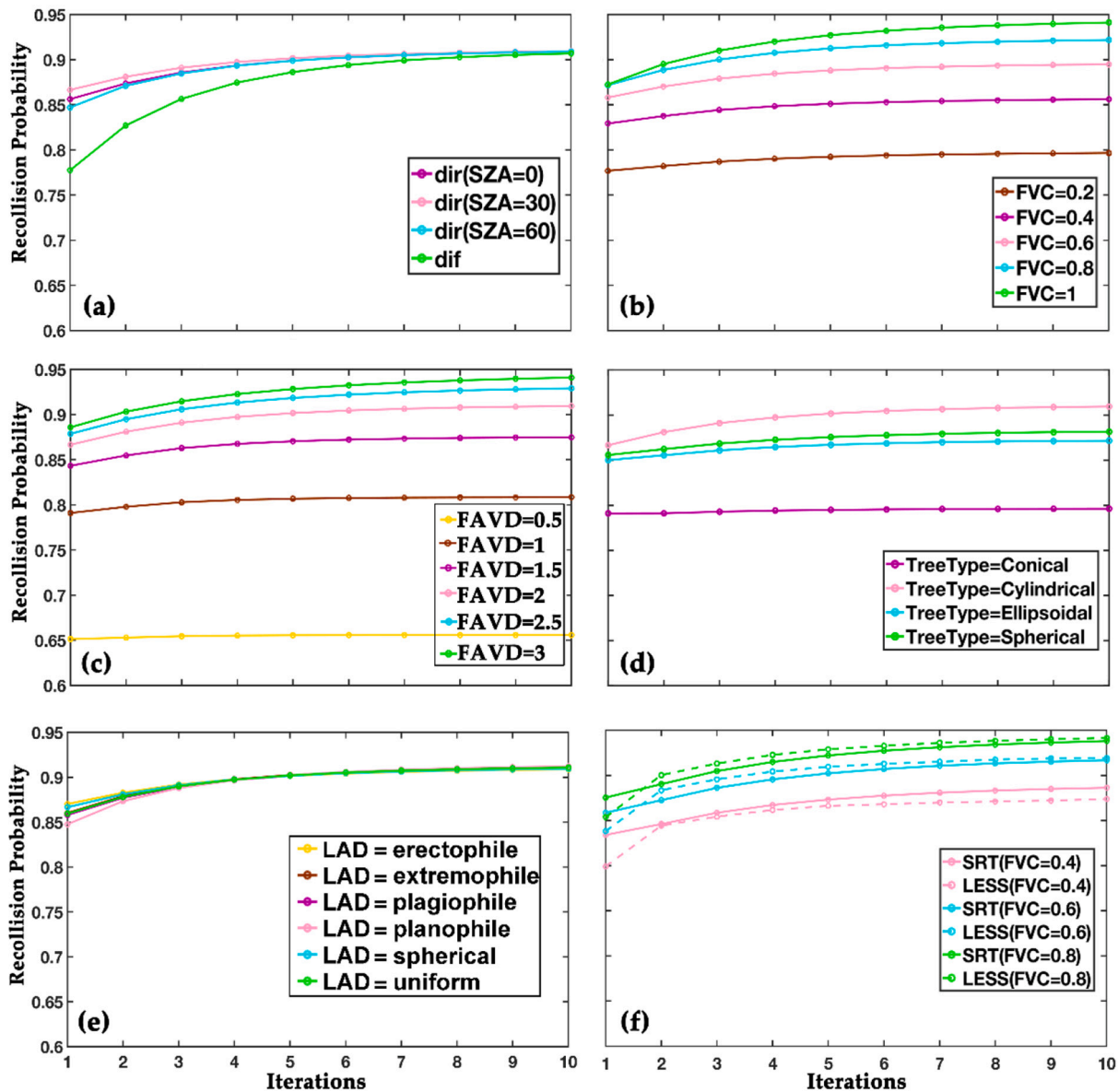


Fig. 7. The recollison probability as a function of multiple scattering iterations when the direct light ratio is 0.7. This function is affected by different parameters and models. The parameters include the solar zenith angle (SZA), upper boundary condition (dir (direct light) and dif (diffused light)) (a), fractional vegetation cover (FVC) (b), foliage area volume density (FAVD) (c), tree types (d), and leaf angle distribution (LAD) (e). Subplot (f) shows the recollison probability simulated by the computer simulation model LESS (dashed lines) and SRT (solid lines) model when FVC are 0.4, 0.6, and 0.8, respectively. In the subplots, the original input parameters include SZA = 30°, SAA = 0°, LAD = spherical, FVC = 0.7, FAVD = 2m²/m³, tree type = cylinder and tree height = 5 m.

in NIR band and decreases in red band (Fig. 8b and c). This can be explained by Table 1, where the soil reflectance is larger than leaf in red band, while the leaf reflectance is larger in NIR band. Besides, we found that the magnitude of reflectance variation gradually decreased when FVC and FAVD increased. This can explain the canopy reflectance saturation (Zhao et al., 2013). In NIR band, we found that Pianophile vegetation has the highest hotspot peak while Erectophile vegetation has the smallest. The reason is that mutual shadowing among leaves is higher for Pianophile leaves (Kallel and Nilson, 2013). In addition, small deviations in the input parameters of vegetation and soil optical properties (T_L, R_L, and R_S) in the model have a significant impact on the model, especially the leaf transmittance. In red band, however, the sensitivity of LAD and optical properties is relatively low (Fig. 8d and f). Compared to other crown types (cylindrical, ellipsoidal, and spherical), the conical crown has a smaller reflectance in NIR band, but a larger reflectance in red band (Fig. 8e). This is because conical canopies are less

able to intercept light than the other three crown types.

3.4. Radiation regime and energy conservation

The result $\bar{I}(z, \Omega)$ obtained by SRTE is the average radiation intensity of the radiation field. Therefore, it is essential to consider the energy conservation of the radiation field to better understand 3D effects of canopy structure on the radiation regime. Here, as shown in Fig. 9, we considered radiation flux density as a canopy depth function. Under different radiative conditions, the radiation flux density of vegetation area (F_U^\uparrow is upward and F_U^\downarrow is downward) and the whole scene (F_I^\uparrow is upward and F_I^\downarrow is downward) varies with the vertical profile. When the diffused light ratio is 0, $F^l(0)$ (downward normalized flux density at top of canopy) is the cosine of the SZA; $F^l(0)$ is 1 when the diffused light ratio is 1. This indicates that the incident radiation flux density is affected by the SZA when the incident radiation includes direct light.

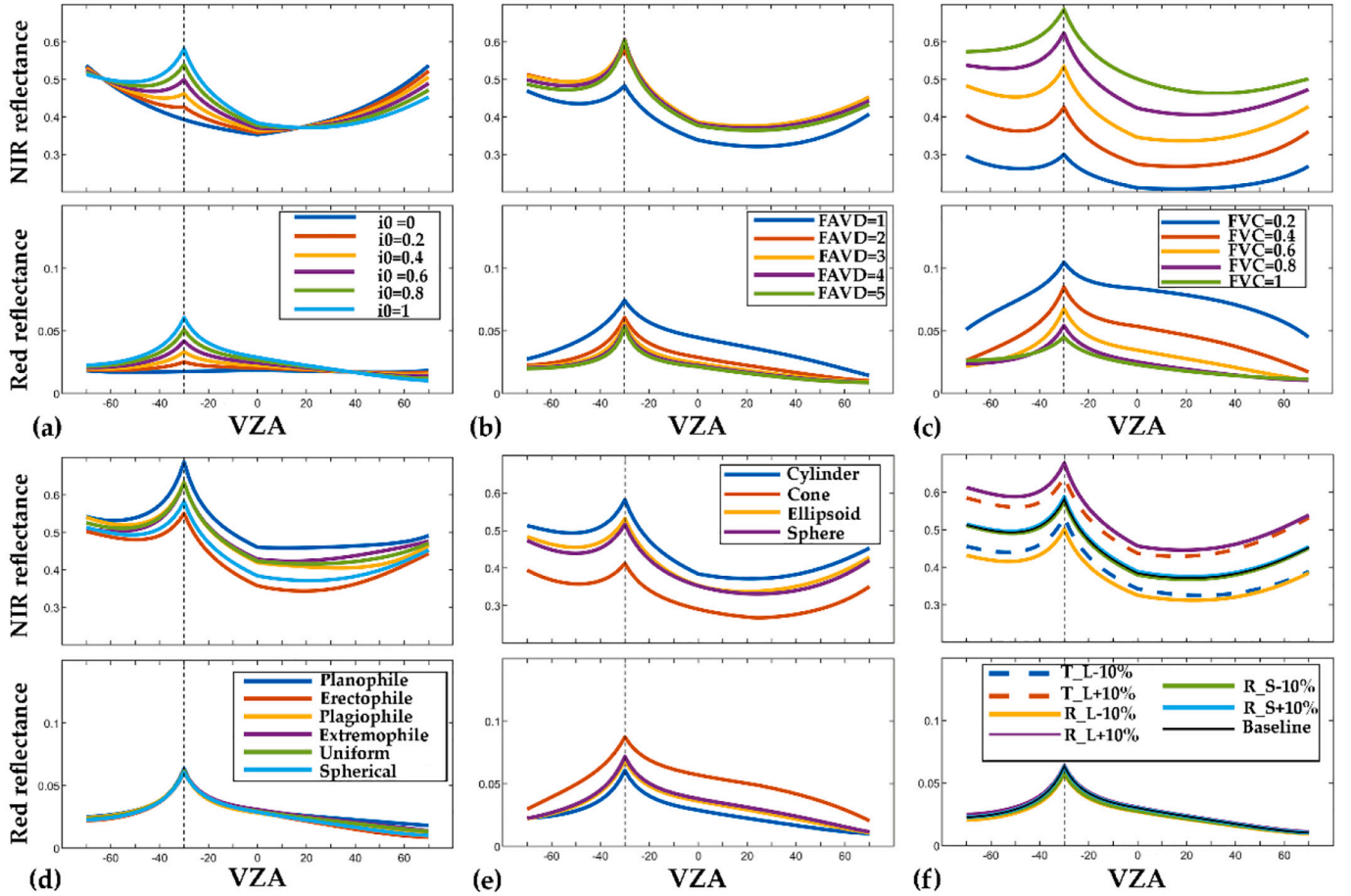


Fig. 8. Sensitivity of reflectances to key factors in the red and NIR bands. The subplots show the influence of direct light ratio (a), foliage area volume density (FAVD) (b), fractional vegetation cover (FVC) (c), leaf angle distribution (LAD) (d), tree type (e) and optical parameters of leaves and soil (f). T_L, R_L, and R_S represent leaf transmittance, leaf reflectance, and soil reflectance, respectively. The upper part of each subplot refers to the red band; the lower part is about the NIR band. The SZA is 30°. The T_L+10%/R_L+10%/R_S+10% and T_L-10%/R_L-10%/R_S-10% refer to leaf transmittance / leaf reflectance / soil reflectance which are increased or decreased 10% of the original transmittance or reflectance. The input parameters include FVC (0.7), FAVD (2m²/m³), tree height (5 m), LAD (spherical) and tree type (cylinder). The optical parameters showed in the Table 1. (For interpretation of the references to colour in this figure legend, the reader is referred to the web version of this article.)

With canopy depth increasing, the attenuation of F_I^{\downarrow} is low compared with that of F_U^{\downarrow} . The main reason is that the whole scene includes both vegetated and non-vegetated areas, but non-vegetated areas do not consume energy. Additionally, as the FVC decreases, the gaps between and within the crown increase, resulting in a decrease in energy attenuation of F_U^{\downarrow} and F_I^{\downarrow} and an increase of soil absorbed flux from the radiation reaching the soil (Zhao et al., 2020). Furthermore, compared with $F^{\downarrow}(0)$ (upward normalized flux density at the top of canopy), $F^{\downarrow}(1)$ (upward normalized flux density when normalized depth is 1) is larger in red band (Fig. 9a and c) but smaller in NIR band (Fig. 9b and d). Both $F^{\downarrow}(0)$ and $F^{\downarrow}(1)$ (downward normalized flux density when the normalized depth is 1) are smaller in red band than in NIR band. The physical explanation for this is that different bands have different spectral characteristics. For example, the red band is dominated by absorption, while the NIR band is dominated by reflectance.

The traditional RT theory follows the energy conservation law. However, the energy conservation law is violated due to the modification of the hotspot effect. Here, we defined the Delta (Eq. (9)) as an indicator to evaluate the whole scene energy conservation. In Fig. 9, $F_I^{\downarrow}(0)$ and $F_I^{\downarrow}(0)$ are the reflected radiation flux density (R) and total incident radiation flux density, respectively. The difference between $F_I^{\downarrow}(0)$ and $F_I^{\downarrow}(0)$ is the sum of transmitted and absorbed radiation flux density (T + A). The R, T, A and the case of energy conservation of the whole scene are calculated when the diffused light ratio changes in

Table 2. Moreover, we found that the energy conservation law is even less satisfied in NIR band compared with red band when the diffused light is 0. The reason for this is that different bands have different optical properties. Most photons are scattered in NIR band, and vegetation hotspot effect should be considered when the photons collide with the vegetation only once.

As described in Section 2.2, the SRT process was split into four subproblems (BS_{Dir}, BS_{Diff}, S_{NoCollision} and S_{Collision}) and the canopy directional reflectance of the whole scene was finally calculated by the above four subproblems and A, T, and R (Table 2). Thus, it is necessary to analyze the energy conservation law for these four subproblems. The diffused light ratio is 0 (Table 3), which means that the subproblem Fig. 2b does not exist. The multiple scattered photons of subproblems BS_{Diff} and S_{Collision} increase as the diffused light ratio (from 0 to 1) increases, leading to a decrease in the hotspot effects (Fig. 2), so the value of Delta is approximate 0. However, the Delta values of BS_{Dir} and S_{NoCollision} are not equal to 0, which means that these parts cannot satisfy the energy conservation law due to the subproblems BS_{Dir} (① and ②-1 in Fig. 2a) and S_{NoCollision} (④ in Fig. 2c) were modified for the hotspot. In addition, compared with NIR band, the “Total” value in red band is smaller, which means that the energy non-conservation phenomenon becomes more significant in NIR band when the diffused light ratio decreases. This is because there is a much stronger multiple scattering in NIR band. The increased energy of one

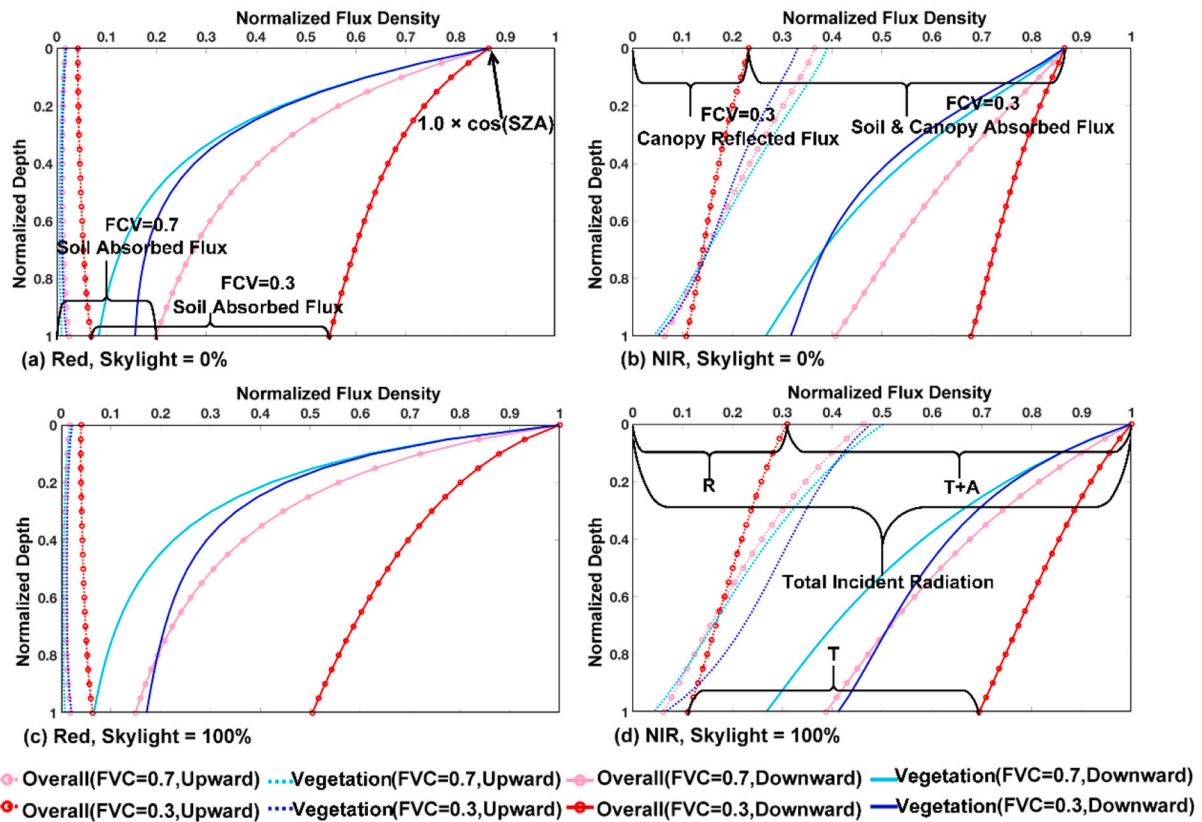


Fig. 9. Radiation regime within a vegetation canopy. When the fractional vegetation cover (FVC) is 0.3 or 0.7, the left panel shows vertical profiles of upward and downward radiation flux densities in red band, while the right panel shows them in NIR band. In the top row, the diffused light ratio is 0, while in the bottom row the diffused light ratio is 1. The solid and dashed lines represent downward and upward flux densities over vegetation, respectively. The solid line with dots represents the downward flux densities of the whole scene and the dashed line with dots represents the total upward flux densities. (For interpretation of the references to colour in this figure legend, the reader is referred to the web version of this article.)

Table 2

Energy conservation (Red/NIR). “Overall” indicates the whole scene, which includes vegetated and non-vegetated areas. The fractional vegetation cover (FVC) of the whole scene is 0.7. The foliage area volume density (FAVD) of the vegetation area is $3m^2/m^3$. The solar zenith angle (SZA) is 30° and the solar azimuth angle (SAA) is 90° . The optical properties of leaf and soil are shown in Table 1.

Skylight	Area	R	T	A	Delta
100%	Overall	0.0157/	0.0310/	0.9560/	-0.26%/
		0.5268	0.1419	0.3363	-0.50%
0%	Overall	0.0161/	0.0477/	0.8109/	-1.01%/
		0.4961	0.1716	0.3001	-11.76%

$$\Delta = (F(0)^{\downarrow} - T - A - R) / F(0)^{\downarrow} \quad (9)$$

where, $F(0)^{\downarrow}$ is the downward flux at the canopy top, R, T, and A are reflected, transmitted, and absorbed radiation flux in the whole scene, respectively.

time scattering in canopy makes the energy conservation even more unsatisfactory.

4. Model validation

4.1. Experiment and data

Three forest plots of $30\text{ m} \times 30\text{ m}$ located in Huailai County, China (40.34° N , 115.78° E), were selected as the experimental area for this study. Each plot is characterized by a discontinuous vegetation canopy

Table 3

Energy conservation for the four subproblems of the SRT processes. When the ratio of incident diffused light changes (0%, 30%, 60%, and 100%), BS_Dir and BS_Dif represent the energy conservation for direct and diffuse in the BS subproblems (Fig. 2a and b). S_NoCollision and S_Collision represent the energy conservation for non-collision and collision in the S subproblem (Fig. 2c and d), respectively. The solar zenith angle (SZA) and solar azimuth angle (SAA) are 30° and 90° , respectively. “Total” is the ratio of remaining energy in the radiation regime of the whole scene, “NaN” denotes that the value does not exist.

Skylight	Delta (Red/NIR)				
	BS_Dir	BS_Dif	S_NoCollision	S_Collision	Total
0%	-0.01%/	NaN	-0.46%/	0.00%/	-1.01%/
	-1.12%		-7.20%	0.00%	-11.75%
30%		0.00%/			-0.62%/
		0.00%			-6.87%
60%					-0.41%/
					-3.56%
100%	NaN				-0.26%/
					-0.50%

represented by a mixture of apricot trees (*Prunus armeniaca L.*) or peach trees (*Prunus persica*). The apricot or peach trees in each plot have different canopy structures (e.g., canopy volume, crown height, etc.) and ages (Fig. 10). The terrain within the plots is relatively flat. The understory is bare clay soil partially covered with scattered senescent leaves and grasses.

The aerial campaigns were performed with an unmanned aerial vehicle (UAV) and collected multi-angular multispectral images over all plots on a cloud-free and windless day (July 2019). The MAPIR survey

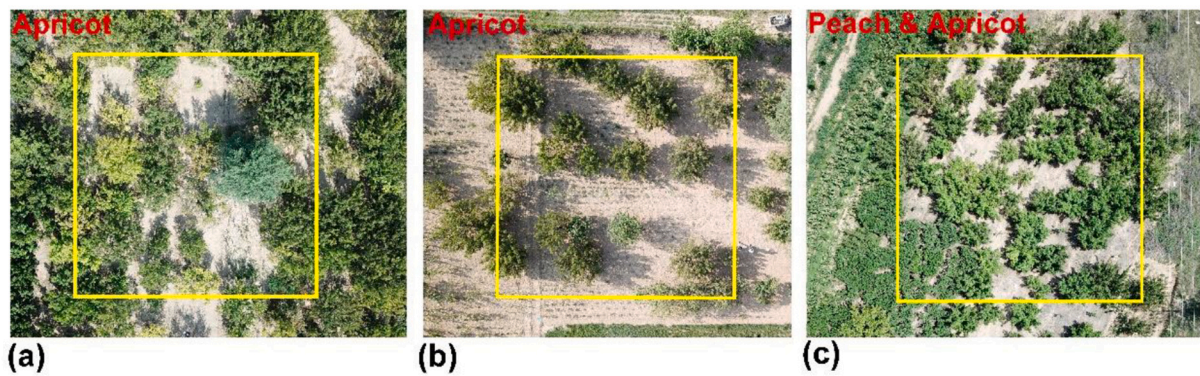


Fig. 10. Discontinuous vegetation canopies consisting of a mixture of apricot (*Prunus armeniaca* L.) or peach (*Prunus presica*) trees in study plots. The trees have different ages and structures. Plot 1 (a) and plot 2 (b) have apricot trees. Plot 3 (c) has peach and apricot trees. The yellow rectangles stand for the study plot borders. (For interpretation of the references to colour in this figure legend, the reader is referred to the web version of this article.)

3N RGN (manufactured by Peau Productions, Inc., San Diego, USA) multispectral camera was mounted on a UAV and a portable ground-based system and recorded three spectral bands with central wavelengths of 550 nm, 660 nm, and 850 nm. The optical axis of the camera was always kept towards the center of the plot during the multi-angular observations. The UAV was programmed to fly at 100 m above ground level, resulting in a footprint of $76 \times 57 \text{ m}^2$ with a ground sampling distance of 2cm when the camera was looking at nadir. The multi-angular missions were launched with two different sun angles for each plot and were taken during an approximately 10-min flight with a goniometric flight pattern along the solar principal plane and perpendicular to the principal plane. The sun moved less than 3° both in zenith and azimuth during the observation period. All UAV-based multispectral images were pre-processed to reflectance with a linear calibration model. Firstly, raw images were imported into MAPIR camera control kernel software and exported into a tagged image file format (TIFF) format. Then, coefficients a and b can be obtained from the linear fit $BRF_n = a \cdot DN_n + b$ based on the relationship between the digital number (DN) values and BRF. Detailed calculation process for coefficients a and b can be found in Li et al. (2021). Finally, the DN values of the NIR image were converted to BRF values. The accurate view-geometry and directional reflectance were derived for each image completely capturing the sample plot. Because the camera employs a Bayer array sensor, the red and green channels were mixed with a certain amount of NIR and thus we did not use these two bands.

At the same time, we measured the spectral reflectance of leaves and soil along with the canopy structure parameters (i.e., average LAI of the scene, crown diameter, tree height, and crown base height) (Table 4). The spectral reflectances of leaf and soil were collected in the nadir direction using an ASD FieldSpec 3 (Analytical Spectral Devices Inc., USA) instrument in a lab. Approximately ten healthy leaf samples were obtained for each plot, and an average reflectance of plots 1 and 2 was taken directly. While the average reflectance of plot 3 was assigned according to the number proportion of different tree species weights. The leaf transmittance was simulated with the PROSPECT model (Jacquemoud and Baret, 1990) and relevant parameters from the model library (e.g., leaf structure parameters, chlorophyll a , chlorophyll b , etc.).

And the reflectance of Lambertian soil was obtained from an average reflectance of some stand. The LAI was measured indirectly using the TRAC optical instrument (3rd Wave Engineering, ON, Canada) along several 30 m transects in the $30 \text{ m} \times 30 \text{ m}$ sample plot. Markers were set every 10 m, and the TRAC manual was referred to operate the TRAC instrument (Hu et al., 2014). The tree crown heights were collected by using a DISTO A5 (Leica Geosystems AG, Heerbrug, Switzerland) hypsometer and a band tape. The crown diameter was measured by averaging two measurements from two measuring tapes laid perpendicular to each other at the largest width of each crown. Undeniably, there were several limitations in our study due to the instrumentation. One limitation stem was that the leaf transmittance was obtained from the PROSPECT model. Although the accuracy of this model has been proven and the model was widely used (Wang et al., 2015), it still did not match the other relevant parameters validated from the field measurements in this study, such as the reflectance of leaf and soil. Another is that we did not obtain reflectance data of three plots in more bands.

4.2. Results

Fig. 11 shows the reflectance of the three study plots of the SRT and 1D RT models as a function of VZA at different moments. The SRT and 1D RT models were compared with the UAV observations. When the VZA is approximated to the SZA, the reflectances from the UAV, the 1D RT and the SRT model have a noticeable hotspot effect. While with the VZA increasing, there is a significant deviation of canopy reflectance values in magnitude and shape between the UAV and SRT and 1D RT, which is because the non-Lambertian soil contribution to the canopy reflectance is essential when the plot FVC is small (Table 4). Additionally, we found an obvious difference between the SRT and 1D RT models in the hotspot direction, and the reflectance from the SRT was closer to the UAV measurements. Furthermore, compared with the 1D RT in other directions, the reflectance from the SRT model was also closer to the UAV measurements. As shown in Fig. 11, the RMSE between SRT and UAV is less than 0.1, while the value between 1D RT and UAV is more than 0.1. The larger RMSE value for 1D RT vs. UAV is attributed to the fact that the 1D RT model treats canopies as homogeneous and ignores

Table 4
Parameters of canopy structure and spectral properties of the three study plots.^a

Plot No.	Structure Parameter						Spectral Parameter (850 nm)		
	Species	LAI	FVC	C_D (m)	C_H (m)	FAVD (m^2/m^3)	L_R	L_T	S_R
1	Apricot	2.36	0.58	3.38	2.87	1.10	0.4485	0.4019	0.3474
2	Apricot	1.71	0.34	3.08	2.26	2.64	0.4767	0.4519	0.3960
3	Peach & Apricot	2.83	0.62	2.99	2.02	2.04	0.4551	0.4319	0.3246

^a C_D, C_H, FAVD, L_R, L_T and S_R are short for crown diameter, crown height, FAVD, leaf reflectance, leaf transmittance and soil reflectance, respectively.

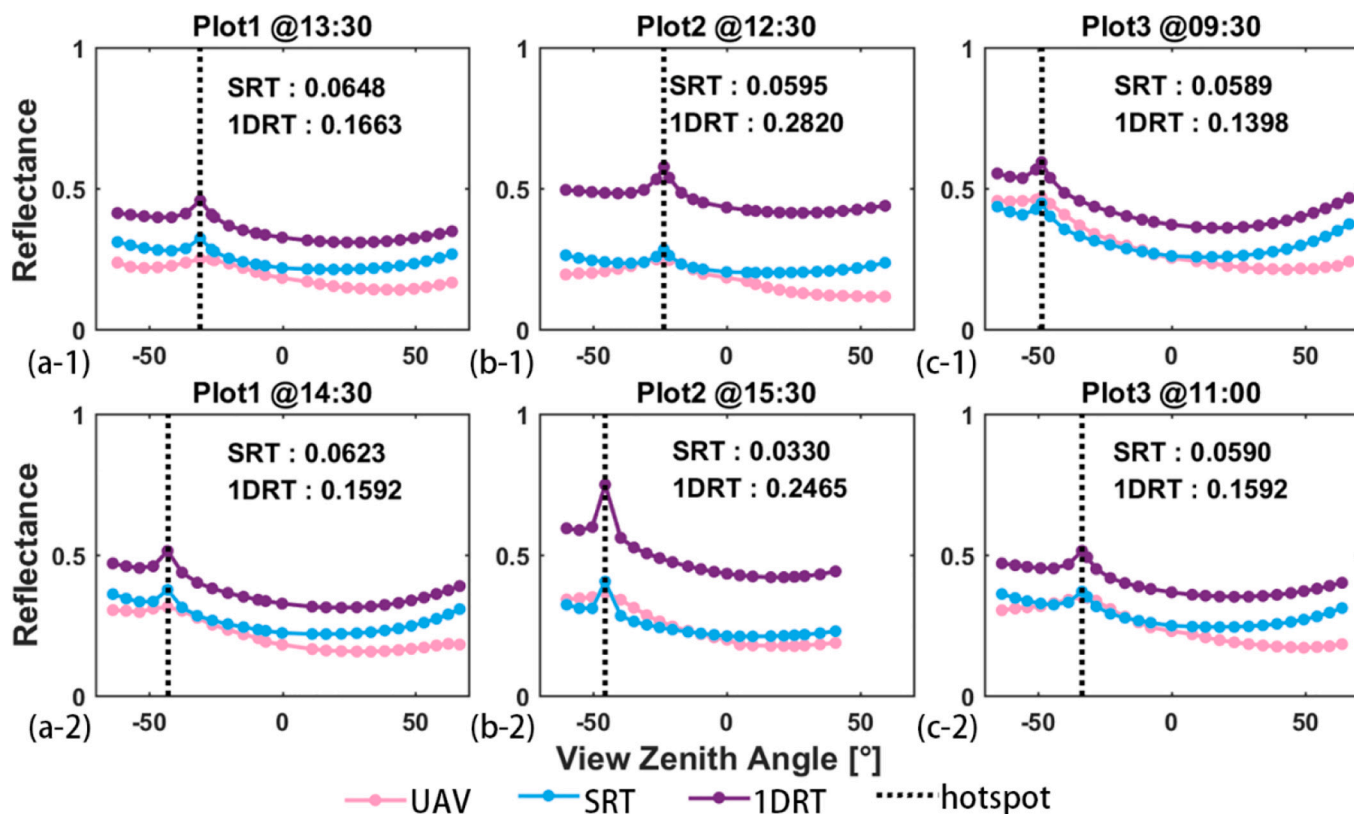


Fig. 11. Comparison of SRT model (blue), 1D RT model (purple), and UAV-measured (pink) reflectances in two observation moments. Plots 1–3 represent three study plots in the principal plane. The black dashed line represents the hotspot direction. The numbers in each subgraph are the root mean square error (RMSE) of the SRT vs. UAV observations and 1D RT vs. UAV observations. (For interpretation of the references to colour in this figure legend, the reader is referred to the web version of this article.)

the gaps between vegetation canopies, which results in a significant overestimation of the scene reflectance. The smaller RMSE value for SRT vs. UAV indicates that the reflectance values of the SRT model are consistent with the field measured using UAV, which is because the SRT model can accurately track the photon trails in the discontinuous canopy. The statistical results overall show that the SRT model can better describe the interaction between the vegetation canopy and radiation in real scenes.

5. Conclusions

Although the SRT theory has been widely adapted to the studies of vegetation canopy, previous version of the SRT model still has two theoretical defects in the hotspot modeling, and the evaluation and validation of the SRT model are still preliminary. Therefore, this article provided a detailed modification for the hotspot problem, and a more comprehensive evaluation, and validation for the SRT model. First, the complete SRT process was divided into four subproblems to analyze and achieve the coupling of SRT and hotspot modeling. By comparing with the SRT_HS2 (our newly proposed SRT-Hotspot coupling scheme), we found that the previous SRT_HS1 incorrectly produced an artificial peak that overestimated the reflectance by up to 16% in hotspot region. Then, this article compared the performance of the modified SRT by comparing multiple intermediate variables (conditional PCF, recollision probability etc.) in the SRT process with 3D computer simulations, and analyzed the model sensitivity to key input parameters as well as the energy spatial distribution and radiation regime conservation. We found that the simulation results of SRT are closer to the well-validated LESS model (RMSE < 0.03 and $R^2 > 0.80$) compared with 1D RT (RMSE < 0.06 and $R^2 > 0.30$). This result indicates that SRT is more accurate than the 1D RT in the discontinuous canopy. We also found that the conditional

PCF based on formula agrees well with Monte Carlo simulation, and it varies with crown types. Moreover, the sensitivity analysis results show that these input parameters (FVC, FAVD, crown type, and LAD) and optical parameters (diffused lights ratio, leaf reflectance, leaf transmittance, and soil reflectance) in the SRT model are sensitive in NIR band than in red band. This model modification results in a violation of the energy conservation in radiation field (e.g., Delta is -11.75% / -0.50% in NIR band and -1.01% / -0.26% in red band when the diffused light ratio is 1 / 0, respectively.). In addition, the UAV observations were used to validate both the SRT and 1D RT models. The results show that the UAV measurements are closer to the SRT compared with the 1D RT, and 1D RT has a significant overestimation. In summary, the SRT model is more suitable for describing the discontinuous canopy than 1D RT. The comprehensive understanding derived from this detailed modification, evaluation and validation of the SRT model provides the basis for further development of radiative transfer theory.

Credit author statement

Kai Yan: Conceptualization, Methodology, Writing - Review & Editing, Funding acquisition, Project administration. Yiman Zhang: Software, Formal analysis, Writing - Original Draft, Investigation, Visualization. Yiyi Tong: Formal analysis and Evaluation. Yelu Zeng: Formal analysis and Evaluation. Jiabin Pu and Si Gao: Software and Investigation. Linyuan Li and Xihan Mu: Validation, Data curation. Guangjian Yan: Methodology. Miina Rautiainen: Conceptualization, Methodology. Yuri Knyazikhin: Supervision, Resources. Ranga B. Myneni: Conceptualization, Resources, Supervision.

Declaration of Competing Interest

The authors declare that they have no known competing financial interests or personal relationships that could have appeared to influence the work reported in this paper.

Acknowledgments

This work was supported by the National Natural Science Foundation of China (Grant No. 41901298, 42090013). We acknowledge all the help from the author of the LESS software, Dr. Jianbo Qi.

Appendix

1. Stochastic Radiative Transfer Equation

The mean intensity $\bar{I}(z, \Omega)$ at depth Z over the whole scene of the horizontal plane can be characterized by Eq. (A1) (Huang et al., 2008):

$$\left\{ \begin{aligned} & \bar{I}(z, \Omega) + \frac{1}{|\mu(\Omega)|} \int_0^z dz' \sigma(\Omega) p(z') \cdot U(z', \Omega) = \\ & \frac{1}{|\mu(\Omega)|} \int_0^z p(z') dz' \int_{4\pi} \sigma_s(\Omega' \rightarrow \Omega) U(z', \Omega') d\Omega' + \bar{I}_0(z, \Omega), \mu(\Omega) < 0 \\ & \bar{I}(z, \Omega) + \frac{1}{|\mu(\Omega)|} \int_z^H dz' \sigma(\Omega) p(z') \cdot U(z', \Omega) = \\ & \frac{1}{|\mu(\Omega)|} \int_z^H p(z') dz' \int_{4\pi} \sigma_s(\Omega' \rightarrow \Omega) U(z', \Omega') d\Omega' + \bar{I}_H(z, \Omega), \mu(\Omega) > 0 \end{aligned} \right. \tag{A1}$$

where $\sigma(\Omega)$ is the extinction coefficient, $\sigma_s(\Omega' \rightarrow \Omega)$ is the differential scattering coefficient, and $\mu(\Omega)$ is the cosine of the polar angle in view direction Ω . $\mu(\Omega) < 0$ ($\mu(\Omega) > 0$) represents the radiation in a downward (upward) direction. $\bar{I}_0(z, \Omega)$ and $\bar{I}_H(z, \Omega)$ are the average radiation intensities over the whole scene of the horizontal plane penetrating the canopy Z through the canopy top and bottom. $p(z)$ is the fractional vegetation cover (FVC) at canopy depth Z (Eq. (A2)). $\chi(x, y, z)$ is the indicator function used to describe the stochastic medium and characterize a stochastic process in space, whose value is 1 if the point (x, y, z) is covered by vegetation and 0 otherwise. This point (x, y, z) travels the distance ζ in the direction Ω to reach (x', y', z') . $\langle \rangle$ denotes the averaging over all possible realizations of $\chi(x, y, z)$ within a finite satellite pixel S_R . The mean intensity $U(z, \Omega)$ at depth Z over the vegetation occupied area of the horizontal plane can be characterized by Eq. A3:

$$p(z) = \left\langle \frac{1}{S_R} \iint_{S_R} \chi(x, y, z) dx dy \right\rangle \tag{A2}$$

$$\left\{ \begin{aligned} & U(z, \Omega) + \frac{1}{|\mu(\Omega)|} \int_0^z dz' \sigma(\Omega) K(z, z', \Omega) \cdot U(z', \Omega) = \\ & \frac{1}{|\mu(\Omega)|} \int_0^z K(z, z', \Omega) dz' \int_{4\pi} \sigma_s(\Omega' \rightarrow \Omega) U(z', \Omega') d\Omega' + U_0(z, \Omega), \mu < 0 \\ & U(z, \Omega) + \frac{1}{\mu(\Omega)} \int_z^H dz' \sigma(\Omega) K(z, z', \Omega) \cdot U(z', \Omega) = \frac{1}{|\mu(\Omega)|} \int_z^H K(z, z', \Omega) dz' \int_{4\pi} \sigma_s(\Omega' \rightarrow \Omega) U(z', \Omega') d\Omega' + U_H(z, \Omega), \mu > 0 \end{aligned} \right. \tag{A3}$$

where $U_0(z, \Omega)$ and $U_H(z, \Omega)$ are the average radiation intensities over the vegetation portion of the horizontal plane penetrating into the canopy Z through the canopy top and bottom. $q(z, z', \Omega)$ is the PCF, or the probability of simultaneously finding vegetation at canopy depth Z and Z' (Eq. (A4)), and $K(z, z', \Omega)$ is the conditional PCF (Eq. (A5)).

$$q(z, z', \Omega) = \left\langle \frac{1}{S_R} \iint_{S_R} \chi(x, y, z) \chi(x', y', z') dx dy \right\rangle \tag{A4}$$

$$K(z, z', \Omega) = \frac{q(z, z', \Omega)}{p(z)} = \left\langle \frac{\iint_{S_R} \chi(x, y, z) \chi(x', y', z') dx dy}{\iint_{S_R} \chi(x, y, z) dx dy} \right\rangle \tag{A5}$$

2. Direct and Diffuse Components

The canopy is illuminated by a direct solar beam and diffuse radiation scattered by the atmosphere. The boundary conditions of the whole scene can be simplified as follows:

$$\bar{I}_0(z, \Omega) = i_0 \delta(\Omega - \Omega_0) + d_0(z, \Omega), \mu < 0 \tag{A6}$$

$$\bar{I}_H(z, \Omega) = d_H(z, \Omega), \mu > 0 \tag{A7}$$

where $\delta(\Omega - \Omega_0)$ is Dirac's delta function, which value is infinity when the polar angle in direction Ω is equal to the direction of direct solar radiation Ω_0 , otherwise, it is 0. i_0 is the intensity of direct radiation incident on the upper boundary. $d_0(z, \Omega)$ and $d_H(z, \Omega)$ are the diffuse radiation intensities incoming from the upper boundary and penetrating the canopy through the lower boundary, respectively.

Therefore, the horizontal average intensity over the vegetation occupied area $U(z, \Omega)$ (Eq. (A3)) can be decomposed into the direct component and the diffuse component of the incoming solar radiation (Shabanov et al., 2000). The direct component $U_{dir}(z)$ and the diffuse component $U_{dif}(z, \Omega)$ are defined:

$$\left\{ \begin{aligned} & U_{dir}(z) + \frac{\sigma(\Omega_0)}{\mu_0} \int_0^z K(z, z', \Omega_0) U_{dir}(z') dz' = 1 \\ & U_{dif}(z, \Omega) + \frac{\sigma(\Omega)}{|\mu|} \int_0^z K(z, z', \Omega) U_{dif}(z', \Omega) dz' = \\ & \frac{1}{|\mu|} \int_0^z K(z, z', \Omega) S_{dif}(z', \Omega) dz' + F_0(z, \Omega), \mu < 0 \\ & U_{dif}(z, \Omega) + \frac{\sigma(\Omega)}{|\mu|} \int_z^H K(z, z', \Omega) U_{dif}(z', \Omega) dz' = \\ & \frac{1}{|\mu|} \int_z^H K(z, z', \Omega) S_{dif}(z', \Omega) dz' + F_H(z, \Omega), \mu > 0 \end{aligned} \right. \tag{A8}$$

where $F_0(z, \Omega)$ and $F_H(z, \Omega)$ are mean sources over foliated point at depth z and direction Ω generated by diffuse and direct radiations incoming through the upper and lower canopy boundaries (Eq. (A9)). $S_{dif}(z', \Omega)$ denotes the spherical integration of scattering:

$$\left\{ \begin{aligned} & F_0(z, \Omega) = i_0 \frac{\sigma_s(\Omega_0 \rightarrow \Omega)}{|\mu|} \int_0^z K(z, z', \Omega) U_{dir}(z') dz' + d_0(z, \Omega), \mu < 0 \\ & F_H(z, \Omega) = i_0 \frac{\sigma_s(\Omega_0 \rightarrow \Omega)}{|\mu|} \int_z^H K(z, z', \Omega) U_{dir}(z') dz' + d_H(z, \Omega), \mu > 0 \\ & S_{dif}(z', \Omega) = \int_{4\pi} \sigma_s(\Omega' \rightarrow \Omega) U_{dif}(z', \Omega') d\Omega' \end{aligned} \right. \tag{A9}$$

The horizontal average intensity over the whole scene area $\bar{I}(z, \Omega)$ (Eq. (A1)) can be decomposed into the direct component and the diffuse component of the incoming solar radiation. The direct component $I_{dir}(z)$ and the diffuse component $I_{dif}(z, \Omega)$ are defined:

$$\left\{ \begin{aligned} & I_{dir}(z) = 1 - \frac{\sigma(\Omega_0)}{|\mu_0|} \int_0^z p(z') U_{dir}(z') dz' \\ & I_{dif}(z, \Omega) = -\frac{\sigma(\Omega)}{|\mu|} \int_0^z p(z') U_{dif}(z', \Omega) dz' + \frac{1}{|\mu|} \int_0^z p(z') S_{dif}(z', \Omega) dz' + \Phi_0(z, \Omega), \mu < 0 \\ & I_{dif}(z, \Omega) = -\frac{\sigma(\Omega)}{|\mu|} \int_z^H p(z') U_{dif}(z', \Omega) dz' + \frac{1}{|\mu|} \int_z^H p(z') S_{dif}(z', \Omega) dz' + \Phi_H(z, \Omega), \mu > 0 \end{aligned} \right. \tag{A10}$$

where $\Phi_0(z, \Omega)$ and $\Phi_H(z, \Omega)$ mean sources over entire horizontal plane at depth z and direction Ω generated by diffuse and direct radiations incoming through the upper and lower canopy boundaries (Eq. (A11)):

$$\left\{ \begin{aligned} & \Phi_0(z, \Omega) = i_0 \frac{\sigma_s(\Omega_0 \rightarrow \Omega)}{|\mu|} \int_0^z p(z') U_{dir}(z') dz' + d_0(\Omega), \mu < 0 \\ & \Phi_H(z, \Omega) = i_0 \frac{\sigma_s(\Omega_0 \rightarrow \Omega)}{|\mu|} \int_z^H p(z') U_{dir}(z') dz' + d_H(\Omega), \mu > 0 \end{aligned} \right. \tag{A11}$$

3. BS and S Problems

According to the full RT problems can be split into two subproblems: (1) black soil (BS) and (2) soil (S), the solution of the full RT model is a

combination of the solutions of the BS and S problem:

$$BRF = BRF_{BS} + \frac{\rho_{soil}}{1 - \rho_{soil} \cdot R_S(\lambda)} T_{BS}(\lambda) \cdot BRF_S \quad (A12)$$

$$\begin{cases} R(\lambda) = R_{BS}(\lambda) + \frac{\rho_{soil}}{1 - \rho_{soil} \cdot R_S(\lambda)} T_{BS}(\lambda) \cdot T_S(\lambda) \\ T(\lambda) = T_{BS}(\lambda) + \frac{\rho_{soil}}{1 - \rho_{soil} \cdot R_S(\lambda)} T_{BS}(\lambda) \cdot R_S(\lambda) \\ A(\lambda) = A_{BS}(\lambda) + \frac{\rho_{soil}}{1 - \rho_{soil} \cdot R_S(\lambda)} T_{BS}(\lambda) \cdot A_S(\lambda) \end{cases} \quad (A13)$$

where $T_{BS}(\lambda)$ and $T_S(\lambda)$ are the canopy transmittances for the BS and S subproblems, respectively. $R_S(\lambda)$ is the canopy albedo for the S problem, λ represents the band, and the bidirectional reflectance factor (BRF) for the BS problem is represented by BRF_{BS} . BRF_{BS} is calculated from the upward radiance and downward irradiance by Eq. (A12):

$$BRF_{BS}(0, \Omega) = \frac{\pi I_{BS}(0, \Omega)}{\mu_0} \quad (A14)$$

where $\mu_0 = \cos \theta_0$ and θ_0 is the solar zenith angle (SZA).

References

- Baret, F., Weiss, M., Lacaze, R., Camacho, F., Makhmara, H., Pacholczyk, P., Smets, B., 2013. GEOV1: LAI and FAPAR essential climate variables and FCOVER global time series capitalizing over existing products. Part1: principles of development and production. *Remote Sens. Environ.* 137, 299–309. <https://doi.org/10.1016/j.rse.2012.12.027>.
- Chen, J.M., Liu, J., Leblanc, S.G., Lacaze, R., Roujean, J., 2003. Multi-angular optical remote sensing for assessing vegetation structure and carbon absorption. *Remote Sens. Environ.* 84, 516–525.
- Clevers, J.G.P.W., 1989. Application of a weighted infrared-red vegetation index for estimating leaf area index by correcting for soil moisture. *Remote Sens. Environ.* 29, 25–37.
- Colombo, R., Bellingeri, D., Fasolini, D., Marino, C.M., 2003. Retrieval of leaf area index in different vegetation types using high resolution satellite data. *Remote Sens. Environ.* 86, 120–131. [https://doi.org/10.1016/S0034-4257\(03\)00094-4](https://doi.org/10.1016/S0034-4257(03)00094-4).
- Comerón, A., Muñoz-Porcar, C., Rocadenbosch, F., Rodríguez-Gómez, A., Sicard, M., 2017. Current research in lidar technology used for the remote sensing of atmospheric aerosols. *Sensors (Switzerland)* 17, 1–16. <https://doi.org/10.3390/s17061450>.
- Diner, D.J., Xu, F., Garay, M.J., Martonchik, J.V., Rheingans, B.E., Geier, S., Davis, A., Hancock, B.R., Jovanovic, V.M., Bull, M.A., Capraro, K., Chipman, R.A., McClain, S. C., 2013. The airborne multiangle SpectroPolarimetric imager (AirMSPD): a new tool for aerosol and cloud remote. *Atmos. Meas. Tech.* 6, 1717–1769.
- Disney, M.I., Lewis, P., North, P.R.J., 2000. Monte Carlo ray tracing in optical canopy reflectance modelling. *Remote Sens. Rev.* 18, 163–196. <https://doi.org/10.1080/02757250009532389>.
- Gastellu-Etchegorry, J.-P., Yin, T., Laurent, N., Cajgfinger, T., Gregoire, T., Grau, E., Feret, J.-B., Lopes, M., Guilleux, J., Dedieu, G., Malenovsky, Z., Cook, B.D., Morton, D., Rubio, J., Durrieu, S., Cazanave, G., Martin, E., Ristorcelli, T., 2015. Discrete anisotropic radiative transfer (DART 5) for modeling airborne and satellite spectroradiometer and LIDAR acquisitions of natural and urban landscapes. *Remote Sens.* 1667–1701.
- Georgi, A.T., 1990. Statistical description of radiation transfer in clouds. *J. Atmos. Sci.* 47, 24–38.
- Goel, N.S., 1988. Models of vegetation canopy reflectance and their use in estimation of biophysical parameters from reflectance data. *Remote Sens. Rev.* 4, 1–212.
- Houborg, R., Soegaard, H., Boegh, E., 2007. Combining vegetation index and model inversion methods for the extraction of key vegetation biophysical parameters using Terra and Aqua MODIS reflectance data. *Remote Sens. Environ.* 106, 39–58. <https://doi.org/10.1016/j.rse.2006.07.016>.
- Hu, R., Yan, G., Mu, X., Luo, J., 2014. Indirect measurement of leaf area index on the basis of path length distribution. *Remote Sens. Environ.* 155, 239–247. <https://doi.org/10.1016/j.rse.2014.08.032>.
- Huang, D., Knyazikhin, Y., Wang, W., Deering, D.W., Stenberg, P., Shabanov, N., Tan, B., Myneni, R.B., 2008. Stochastic transport theory for investigating the three-dimensional canopy structure from space measurements. *Remote Sens. Environ.* 112, 35–50.
- Huang, C., Chen, Y., Zhang, S., Wu, J., 2018. Detecting, extracting, and monitoring surface water from space using optical sensors: a review. *Rev. Geophys.* 56, 333–360. <https://doi.org/10.1029/2018RG000598>.
- Jacquemoud, S., Baret, F., 1990. PROSPECT: a model of leaf optical properties spectra. *Remote Sens. Environ.* 34, 75–91. [https://doi.org/10.1016/0034-4257\(90\)90100-Z](https://doi.org/10.1016/0034-4257(90)90100-Z).
- Jacquemoud, S., Bacour, C., Poilve, H., 1997. Comparison of four radiative transfer models to simulate plant canopies reflectance: direct and inverse mode. *Remote Sens. Environ.* 4257.
- Jawak, S.D., Luis, A.J., 2013. Improved land cover mapping using high resolution multiangle 8-band WorldView-2 satellite remote sensing data satellite remote sensing data. *J. Appl. Remote. Sens.* 7, 073573.
- Jiao, W., Zhang, L., Chang, Q., Fu, D., Cen, Y., Tong, Q., 2016. Evaluating an enhanced vegetation condition index (VCI) based on VIUPD for drought monitoring in the continental United States. *Remote Sens.* 8, 224.
- Kallel, A., Nilson, T., 2013. Revisiting the vegetation hot spot modeling: case of Poisson/binomial leaf distributions. *Remote Sens. Environ.* 130, 188–204. <https://doi.org/10.1016/j.rse.2012.11.018>.
- Kern, A., Marjanović, H., Barcza, Z., 2020. Spring vegetation green-up dynamics in Central Europe based on 20-year long MODIS NDVI data. *Agric. For. Meteorol.* 287, 107969. <https://doi.org/10.1016/j.agrformet.2020.107969>.
- Knyazikhin, Y., Martonchik, J.V., Myneni, R.B., Diner, D.J., Running, S.W., 1998. Synergistic algorithm for estimating vegetation canopy leaf area index and fraction of absorbed photosynthetically active radiation from MODIS and MISR data. *J. Geophys. Res.* pp. 32257–32275.
- Knyazikhin, Y., Schull, M.A., Xu, L., Myneni, R.B., Samanta, A., 2011. Canopy spectral invariants. Part 1: a new concept in remote sensing of vegetation. *J. Quant. Spectrosc. Radiat. Transf.* 112, 727–735. <https://doi.org/10.1016/j.jqsrt.2010.06.014>.
- Kotchenova, S.Y., Shabanov, N.V., Knyazikhin, Y., Davis, A.B., Dubayah, R., Myneni, R. B., 2003. Modeling lidar waveforms with time-dependent stochastic radiative transfer theory for remote estimations of forest structure. *J. Geophys. Res. Atmos.* 108, 4484.
- Kuusik, A., 1985. The hot spot effect of a uniform vegetative cover. *Sov. J. Remote. Sens.* 3, 645–658.
- Lechner, A.M., Foody, G.M., Boyd, D.S., 2020. Applications in remote sensing to forest ecology and management. *One Earth* 2, 405–412. <https://doi.org/10.1016/j.oneear.2020.05.001>.
- Lee, B., Kwon, H., Miyata, A., Lindner, S., Tenhunen, J., 2017. Evaluation of a phenology-dependent response method for estimating leaf area index of rice across climate gradients. *Remote Sens.* 9, 1–16.
- Lewis, P., Disney, M., 2007. Spectral invariants and scattering across multiple scales from within-leaf to canopy. *Remote Sens. Environ.* 109, 196–206.
- Li, X., Huang, H., Shabanov, N.V., Chen, L., Yan, K., Shi, J., 2020. Extending the stochastic radiative transfer theory to simulate BRF over forests with heterogeneous distribution of damaged foliage inside of tree crowns. *Remote Sens. Environ.* 250, 112040.
- Li, L., Mu, X., Qi, J., Pisek, J., Roosjen, P., Yan, G., Huang, H., Liu, S., Baret, F., 2021. Characterizing reflectance anisotropy of background soil in open-canopy plantations using UAV-based multiangular images. *ISPRS J. Photogramm. Remote Sens.* 177, 263–278. <https://doi.org/10.1016/j.isprsjprs.2021.05.007>.
- Möttus, M., 2007. Photon recollision probability in discrete crown canopies. *Remote Sens. Environ.* 110, 176–185.
- Peral, E., Im, E., Wye, L., Lee, S., Tanelli, S., Rahmat-Samii, Y., Horst, S., Hoffman, J., Yun, S.H., Imken, T., Hawkins, D., 2018. Radar technologies for earth remote sensing from CubeSat platforms. *Proc. IEEE* 106, 404–418. <https://doi.org/10.1109/JPROC.2018.2793179>.
- Pu, J., Yan, K., Zhou, G., Lei, Y., Zhu, Y., Guo, D., Li, H., Xu, L., Knyazikhin, Y., Myneni, R.B., 2020. Evaluation of the MODIS LAI/FPAR algorithm based on 3D-RTM simulations: a case study of grassland. *Remote Sens.* 12, 3391. <https://doi.org/10.3390/rs12203391>.
- Qi, J., Xie, D., Yin, T., Yan, G., Gastellu-Etchegorry, J.P., Li, L., Zhang, W., Mu, X., Norford, L.K., 2019. LESS: Large-scale remote sensing data and image simulation framework over heterogeneous 3D scenes. *Remote Sens. Environ.* 221, 695–706.

- Qin, W., Xiang, Y., 1994. On the hotspot effect of leaf canopies: modeling study and influence of leaf shape. *Remote Sens. Environ.* 50, 95–106. [https://doi.org/10.1016/0034-4257\(94\)90037-X](https://doi.org/10.1016/0034-4257(94)90037-X).
- Rasmus, H., Joshua, B.F., Skidmore, K., 2015. International journal of applied earth observation and geoinformation. *Int. J. Appl. Earth Obs. Geoinf.* 43, 1–6. <https://doi.org/10.1016/j.jag.2015.06.001>.
- Ross, J., Marshak, A., 1989. The influence of leaf orientation and the specular component of leaf reflectance on the canopy bidirectional reflectance. *Remote Sens. Environ.* 27, 251–260.
- Shabanov, N.V., Knyazikhin, Y., Baret, F., Myneni, R.B., 2000. Stochastic modeling of radiation regime in discontinuous vegetation canopies. *Remote Sens. Environ.* 74, 125–144.
- Shabanov, N.V., Huang, D., Yang, W., Tan, B., Knyazikhin, Y., Myneni, R.B., Ahl, D.E., Gower, S.T., Huete, A.R., Aragão, L.E.O.C., Shimabukuro, Y.E., Broadleaf, A., 2005. Analysis and Optimization of the MODIS Leaf Area Index Algorithm Retrievals Over Broadleaf Forests, 43, pp. 1855–1865.
- Shabanov, N.V., Huang, D., Knjazikhin, Y., Dickinson, R.E., Myneni, R.B., 2007. Stochastic radiative transfer model for mixture of discontinuous vegetation canopies. *J. Quant. Spectrosc. Radiat. Transf.* 107, 236–262.
- Shibayama, M., Wiegand, C.L., 1985. View azimuth and zenith, and solar angle effects on wheat canopy reflectance. *Remote Sens. Environ.* 18, 91–103.
- Smolander, S., Stenberg, P., 2005. Simple parameterizations of the radiation budget of uniform broadleaved and coniferous canopies. *Remote Sens. Environ.* 94, 355–363.
- Suits, G.H., 1971. The calculation of the directional reflectance of a vegetative canopy. *Remote Sens. Environ.* 2, 117–125.
- Tian, Y., Wang, Y., Zhang, Y., Knyazikhin, Y., Bogaert, J., Myneni, R.B., 2003. Radiative transfer based scaling of LAI retrievals from reflectance data of different resolutions. *Remote Sens. Environ.* 84, 143–159. [https://doi.org/10.1016/S0034-4257\(02\)00102-5](https://doi.org/10.1016/S0034-4257(02)00102-5).
- Vainikko, G.M., 1973a. The equation of mean radiance in broken cloudiness. *Tr. Mosk. Gos. Kom. SSSR Meteorol. Invest* 21, 28–37.
- Vainikko, G.M., 1973b. Transfer approach to the mean intensity of radiation in non-continuous clouds. *Tr. MGK SSSR. Meteorol. Investig.* 21, 28–37.
- Venturini, V., Bisht, G., Islam, S., Jiang, L., 2004. Comparison of evaporative fractions estimated from AVHRR and MODIS sensors over South Florida. *Remote Sens. Environ.* 93, 77–86. <https://doi.org/10.1016/j.rse.2004.06.020>.
- Verheof, W., 1984. Light scattering by leaf layers with application to canopy reflectance modeling: the SAIL model. *Remote Sens. Environ.* 141, 125–141.
- Verrelst, J., Muñoz, J., Alonso, L., Delegido, J., Rivera, J.P., Camps-Valls, G., Moreno, J., 2012. Machine learning regression algorithms for biophysical parameter retrieval: opportunities for Sentinel-2 and -3. *Remote Sens. Environ.* 118, 127–139. <https://doi.org/10.1016/j.rse.2011.11.002>.
- Vuolo, F., Neugebauer, N., Bolognesi, S.F., Atzberger, C., D'Urso, G., 2013. Estimation of leaf area index using DEIMOS-1 data: application and transferability of a semi-empirical relationship between two agricultural areas. *Remote Sens.* 5, 1274–1291. <https://doi.org/10.3390/rs5031274>.
- Walthall, C.L., Norman, J.M., Welles, J.M., Campbell, G., Blad, B.L., 1985. Simple equation to approximate the bidirectional reflectance from vegetative canopies and bare soil surfaces. *Opt. Soc.* 24, 383–387.
- Shabanov, N.V., Wang, Y., Buermann, W., Dong, J., Hoffman, S., Smith, G.R., Tian, Y., Knyazikhin, Y., Myneni, R.B., 2003. Effect of Foliage Spatial Heterogeneity in the MODIS LAI and FPAR Algorithm over Broadleaf Forests, 85, pp. 410–423. [https://doi.org/10.1016/S0034-4257\(03\)00017-8](https://doi.org/10.1016/S0034-4257(03)00017-8).
- Wang, Z., Skidmore, A.K., Wang, T., Darvishzadeh, R., Hearne, J., 2015. Applicability of the PROSPECT model for estimating protein and cellulose + lignin in fresh leaves. *Remote Sens. Environ.* 168, 205–218. <https://doi.org/10.1016/j.rse.2015.07.007>.
- Xiao, Y., Zhao, W.J., Zhou, D.M., Gong, H.L., 2014. Sensitivity analysis of vegetation reflectance to biochemical and biophysical variables at leaf, canopy, and regional scales. *IEEE Int. Geosci. Remote Sens. Symp.* 52, 4014–4024.
- Xiao, Z., Liang, S., Wang, J., Chen, P., Yin, X., Zhang, L., Song, J., 2014. Use of general regression neural networks for generating the GLASS leaf area index product from time-series MODIS surface reflectance. *IEEE Trans. Geosci. Remote Sens.* 52, 209–223. <https://doi.org/10.1109/TGRS.2013.2237780>.
- Yan, K., Park, T., Yan, G., Chen, C., Yang, B., Liu, Z., Nemani, R.R., Knyazikhin, Y., Myneni, R.B., 2016a. Evaluation of MODIS LAI/FPAR product collection 6. Part 1: consistency and improvements. *Remote Sens.* 8, 1–16. <https://doi.org/10.3390/rs8050359>.
- Yan, K., Park, T., Yan, G., Liu, Z., Yang, B., Chen, C., Nemani, R.R., Knyazikhin, Y., Myneni, R.B., 2016b. Evaluation of MODIS LAI/FPAR product collection 6. Part 2: validation and intercomparison. *Remote Sens.* 8. <https://doi.org/10.3390/rs8060460>.
- Yan, K., Park, T., Chen, C., Xu, B., Song, W., Yang, B., Zeng, Y., Liu, Z., Yan, G., Knyazikhin, Y., Myneni, R.B., 2018. Generating global products of LAI and FPAR from SNPP-VIIRS data: theoretical background and implementation. *IEEE Trans. Geosci. Remote Sens.* 56, 2119–2137. <https://doi.org/10.1109/TGRS.2017.2775247>.
- Yan, G., Chu, Q., Tong, Y., Mu, X., Qi, J., Zhou, Y., Liu, Y., Wang, T., Xie, D., Zhang, W., Yan, K., Chen, S., Zhou, H., 2021. An operational method for validating the downward shortwave radiation over rugged terrains. *IEEE Trans. Geosci. Remote Sens.* 59, 714–731. <https://doi.org/10.1109/TGRS.2020.2994384>.
- Yan, K., Gao, S., Chi, H., Qi, J., Song, W., Tong, Y., Mu, X., Yan, G., 2021a. Evaluation of the vegetation-index-based dimidiate pixel model for fractional vegetation cover estimation. *IEEE Trans. Geosci. Remote Sens.* 1–14. <https://doi.org/10.1109/TGRS.2020.3048493>.
- Yan, K., Pu, J., Park, T., Xu, B., Zeng, Y., Yan, G., Weiss, M., Knyazikhin, Y., Myneni, R.B., 2021b. Performance stability of the MODIS and VIIRS LAI algorithms inferred from analysis of long time series of products. *Remote Sens. Environ.* 260, 112438. <https://doi.org/10.1016/j.rse.2021.112438>.
- Yan, K., Zou, D., Yan, G., Fang, H., Weiss, M., Rautiainen, M., Knyazikhin, Y., Myneni, R. B., 2021c. A bibliometric visualization review of the MODIS LAI/FPAR products from 1995 to 2020. *J. Remote Sens.* 2021, 7410921. <https://doi.org/10.34133/2021/7410921>.
- Yang, B., Knyazikhin, Y., Möttus, M., Rautiainen, M., Stenberg, P., Yan, L., Chen, C., Yan, K., Choi, S., Park, T., Myneni, R.B., 2017. Estimation of leaf area index and its sunlit portion from DSCOVR EPIC data: theoretical basis. *Remote Sens. Environ.* 198, 69–84. <https://doi.org/10.1016/j.rse.2017.05.033>.
- Yin, G., Li, J., Liu, Q., Fan, W., Xu, B., Zeng, Y., Zhao, J., 2015. Regional Leaf Area Index Retrieval Based on Remote Sensing: The Role of Radiative Transfer Model Selection, pp. 4604–4625. <https://doi.org/10.3390/rs70404604>.
- Yin, G., Li, A., Zhao, W., Jin, H., Bian, J., Wu, S., 2017. Modeling canopy reflectance over sloping terrain based on path length correction. *IEEE Trans. Geosci. Remote Sens.* 55, 4597–4609. <https://doi.org/10.1109/TGRS.2017.2694483>.
- Zeng, Y., Badgley, G., Chen, M., Li, J., Anderegg, L.D.L., Kornfeld, A., Liu, Q., Xu, B., Yang, B., Yan, K., Berry, J.A., 2020a. A radiative transfer model for solar induced fluorescence using spectral invariants theory. *Remote Sens. Environ.* 240, 111678. <https://doi.org/10.1016/j.rse.2020.111678>.
- Zeng, Y., Li, J., Liu, Q., Huete, A.R., Xu, B., Yin, G., Fan, W., Ouyang, Y., Yan, K., Hao, D., Chen, M., 2020b. A radiative transfer model for patchy landscapes based on stochastic radiative transfer theory. *IEEE Trans. Geosci. Remote Sens.* 58, 2571–2589. <https://doi.org/10.1109/TGRS.2019.2952377>.
- Zhao, J., Li, J., Liu, Q., 2013. Analysis on inversion saturation of leaf area index based on multi-layer models. In: *International Geoscience and Remote Sensing Symposium (IGARSS)*. IEEE, pp. 3048–3051. <https://doi.org/10.1109/IGARSS.2013.6723469>.
- Zhao, J., Li, J., Liu, Q., Xu, B., Yu, W., Lin, S., Hu, Z., 2020. Estimating fractional vegetation cover from leaf area index and clumping index based on the gap probability theory. *Int. J. Appl. Earth Obs. Geoinf.* 90, 102112. <https://doi.org/10.1016/j.jag.2020.102112>.